Chapter 2

Detector for the Linear Collider

General Detector Concepts and Detector Performance

Conveners: M. Martinez, D.J. Miller, M. Piccolo

Working Group: A. Andreazza, M. Battaglia, G. Blair, G. Daskalakis, A. Juste, A. Kyriakis, C. Markou, H.U. Martyn, H. Nowak, I. Riu, M. Sachwitz, H.J. Schreiber, D. Schulte, R. Settles, R. Shanidze, C. Shepherd-Themistocleous, S. Shichanin, E. Simopoulou, R. Vuopionperä, C. Troncon

Detector Subsystems

Conveners: M. Mazzucato, D. Saxon, R. Settles

Working Group: S. Aïd, A. Andreazza, P. Bambade, T. Barklow, W. Bartel, M. Battaglia, R. Bellanzzini, S. Bertolucci, G. Blair, R. Brinkmann, I. Brock, R. Brown, J. Bürger, P.J. Bussey, M. Caccia, P. Checchia, G. Coignet, P. Colas, P. Clarke, C. Damerell, M. David, A. De Roeck, E. Elsen, E. Fernandez, Y. Giomataris, T. Greenshaw, R. Heuer, C. Heusch, N. Holtkamp, P. Hüntemeyer, P. Janot, L. Jönsson, F.P. Juster, B.J. King, F. Kircher, V. Korbel, U. Kötz, Y. Kurihara, P. Le Du, M. Leenen, W. Lohmann, C. Luci, L. Mandelli, M. Martinez, C. Meroni, J. Meyer, D. Miller, R. Nahnhauer, O. Napoly, R. Nania, R. Orava, M. Piccolo, M. Pohl, D. Reed, F. Richard, A. Rousarie, H.-G. Sander, U. Schneekloth, H.J. Schreiber, S. Schreiber, D. Schulte, C. Shepherd-Themistocleous, F. Simonetto, K. Sinram, A. Skillman, A. Sopczak, P. Steffen, H. Steiner, J. Steuerer, G. Tonelli, M. Tonutti, C. Troncon, C. VanderVelde, G. Vegni, A. Wagner, N. Walker, M. Weber, W. Wiedenmann, G.W. Wilson, K. Zapfe-Düren

Collider-Experiment Interface

Conveners: N. Holtkamp, M. Leenen, O. Napoly

Working Group: G. Bardin, R. Brinkmann, C. Cavata, S. Drozhdin, J.-P. Jorda, N. Mokhov, M. Sachwitz, H.J. Schreiber, S. Schreiber, D. Schulte, R. Settles, K. Sinram, N. Walker, K. Zapfe-Düren

Contents

2.3 Detector Performance

In order to assess the physics capabilities of the detector described earlier in this document, a few reference reactions have been analyzed in detail:

- $e^+e^- \to t\bar{t}$ at threshold
- $e^+e^- \to H^0Z^0$ at $\sqrt{s} = 360, 500\,\mathrm{GeV}$
- $e^+e^- \to HA$ at $\sqrt{s} = 800\,\mathrm{GeV}$
- $e^+e^- \to WW \to \ell\nu q\bar{q}$ at $\sqrt{s} = 500\,\mathrm{GeV}$,
- $e^+e^- \to \tilde{\chi}_1^+\tilde{\chi}_1^-$ at $\sqrt{s} = 500\,\mathrm{GeV}$
- $e^+e^- \to \tilde{\mu}_R\tilde{\mu}_R$ at $\sqrt{s} = 800\,\mathrm{GeV}$

The rationale for choosing the reactions listed above can be summarized as follows:

- The study of top production at threshold tests the ability of the detector to cope with multijet events and to reconstruct the invariant masses needed to identify top events; furthermore, the beamstrahlung associated with the beam-beam interaction at the IP, has to be evaluated and shown not to spoil the expected mass resolution for the top quark mass measurement.
- Higgs production and branching ratio measurements are connected with b-tagging and tracking performances of the experimental set-up.
- Again H and A bosons detection requires good b detection together with jets energy and direction determination in order to form jet-jet invariant masses.
- WW production allows to determine the optimal angular coverage of the detector as the W-pair angular distribution peaks in the very forward region.
- Sleptons and/or charginos detection tests the di-jet mass resolution, the capability of the detector in the measurement of missing energy, and lepton identification.

In addition to these processes, the measurement of the luminosity and of the center of mass energy has been also studied since their precise knowledge is crucial for the other measurements. In the following the performance of the detector subsystems is analyzed in some detail: the relevant processes were simulated with generators, which are thought reasonably accurate as of now; detector smearing was obtained with SIMDET code [1]. This software package returns momenta and energies of isolated particles; charged prongs and/or neutral entering the calorimeters with relative distances smaller than the proposed granularity are combined into *energy clusters*. The isolation cut is hence set by the cell geometry of the proposed calorimeters. Particle clusters undergo separate smearing for the e.m. and hadronic components of the energy. Smeared energies are then combined into *total cluster energy*. Minimum energy/momentum cuts are set at 200 MeV/c (p_t tracking) and 100/300 MeV for the e.m./hadronic calorimeters. Misidentifications π/μ and π/e were implemented at the usual level. Complete GEANT simulation was used if the details of the detector response were believed important (e.g. heavy flavor tagging). The detail of the analyses and the results are discussed in the following paragraphs.

2.3.1 Precision Measurement of Luminosity and $\sqrt{s}$

2.3.1.1 Motivation

To realize the full physics potential of the linear collider, for example in accurate measurements of the W boson and top quark masses, it will be necessary to develop precise techniques for measuring the integrated luminosity, the center of mass energy and the luminosity spectrum as a function of $\sqrt{s}$. External spectrometers (see section 2.4.6.2) for the outgoing beam can be used to measure the energies of the un-interacted beams, but they can not measure the true spectrum at interaction. Beamstrahlung spreads the luminosity over a range of energies and shifts the peak value of $\sqrt{s}$ at interaction away from precisely $2E_{\mathrm{beam}}$. These effects can only be monitored reliably by analyzing samples of calibration events taken from the same datasets as the events used for physics studies.

2.3.1.2 Absolute Energy Measurement

The most useful quantity available for calibrating the energy is the mass of the Z-boson [2]; measured at LEP with a precision of a few MeV. The cross section for $\mathrm{e^+e^-} \to \mathrm{Z}\gamma$ is comparable with the WW cross section and significantly larger than that for $\mathrm{t\bar{t}}$. The most precise determination of energy will come from kinematic fits to events with $\mathrm{Z} \to \mu^+\mu^-$ and with the radiated photon lost along the beam direction. There is an inescapable error from the width of the Z boson:

$$\frac{\Delta(\sqrt{s})}{\sqrt{s}} = \frac{5 \cdot 10^{-4} \times (\sqrt{s}/161)}{\sqrt{f_{\mathrm{acc}}\mathcal{L}(\mathrm{fb}^{-1})}} \tag{2.3.1}$$

where f_{acc} is the fractional acceptance of the detector for $\mathrm{Z} \to \mu^+\mu^-$. With the outer cone of the forward shielding mask at 83 mrad, $f_{\mathrm{acc}} \simeq 1$ for $\sqrt{s} \leq 500$ GeV and drops to 0 for $\sqrt{s} \simeq 2$ TeV. This gives $\Delta(\sqrt{s})/\sqrt{s} = 1.6 \cdot 10^{-4}$ for 10 fb^{-1} at $\sqrt{s} = 161$ GeV. For each event the contribution to the error from the angular resolution on the muon tracks must be kept below a half of the contribution from the width of the Z, requiring an angular resolution of 3 mrad on muons at $\theta \simeq 60°$ for $\sqrt{s} = 161$ GeV, or 200 μrad at

$\theta \simeq 190\,\mathrm{mrad}$ for $\sqrt{s} = 1\,\mathrm{TeV}$. These measurement errors can easily be achieved with the detector described in this chapter, using the intermediate silicon layer and TPC for large angle muons or the forward silicon tracker for muons close to the shielding mask.

2.3.1.3 Integrated Luminosity Measurement

Because of the large flux of soft electrons and gamma rays coming from the interaction point it is not clear that the small-angle luminosity monitors (see section 2.2.7), inside the shielding mask, will be able to perform as well as the equivalent detectors in the LEP experiments which are now achieving systematic errors of much less than 1 per mille. This is one of the R&D projects which needs to be pursued as the design develops. Such a small angle monitor is needed for a number of physics reasons, especially for tagging gamma-gamma scattering events and to give the best possible hermeticity for high energy electrons and gamma rays. But away from the Z boson peak it may also be possible to normalize on larger angle Bhabha scatters. The number of events with e^+e^- going outside the mask is much higher than any physics channel, so statistics will not be a significant limitation on the precision of measuring the integrated luminosity. Studies at CLEO [3], however, have shown that the systematic errors on the theoretical cross sections limit the precision available at the present time to a little less than 1 %. But the same was true for the Bhabha cross sections at small angles when LEP1 first began using them for luminosity measurement and significant improvements have since been made which have almost matched the improvements in experimental errors. Theorists [4] who have worked on the LEP luminosity have no doubt that similar improvements can be made to the cross section calculations for larger angles. This will require a substantial effort from the theory community.

2.3.1.4 Measuring the Luminosity Spectrum

The spread of $\sqrt{s}$ due to beamstrahlung, initial state radiation and the momentum spread in the linacs can be directly related [5] to the distribution of the acollinearity of the e^+ and e^- in Bhabha scattering events outside the shielding cone. Recent studies at KEK [6] have confirmed that the effects of realistic beamstrahlung distributions can indeed be resolved in this way. In order to achieve the precision needed for measuring the top quark mass to better than 200 MeV in the scan over the $t\bar{t}$ threshold (see section 2.3.2.2) it will be necessary to measure the angle θ of the e^+ and e^- tracks to better than $250\,\mu\mathrm{rad}$ for $\theta \simeq 180\,\mathrm{mrad}$ or to better than $1\,\mathrm{mrad}$ for $300 < \theta < 800\,\mathrm{mrad}$; similar requirements to those mentioned above in the discussion of energy measurement (section 2.3.1.2). They should be easily achieved in this detector, as long as the amount of material in front of the precision detectors is kept to a small fraction of a radiation length so that electrons do not shower before their tracks can be measured. Good electron identification will be needed in the endcaps.

2.3.2 Top Physics

One of the main physics topics for the next generation colliders (both e^+e^- and hadronic) will be the production and properties of the top quark. An e^+e^- collider is particularly suited to study in detail top quark physics thanks to the extreme cleanliness of the leptonic environment. Top quarks will be copiously pair-produced at such a machine and, since they are heavier than the intermediate vector bosons, (maybe even heavier than the Higgs boson), their properties will be different from the ones of the lighter quarks; as a matter of fact they might shed some light on the mechanism of mass generation and provide valuable information for the understanding of flavor symmetries. The dominant top production channel goes through the e^+e^- annihilation to a virtual photon or Z, which subsequently decays to a $t\bar{t}$ pair. The $t\bar{t}$ production cross section is about 650 fb at $\sqrt{s} = 500\,\mathrm{GeV}$. At the foreseen luminosities of 10^{33} to $10^{34}\,\mathrm{cm}^{-2}\mathrm{s}^{-1}$ (or 10 to 100 fb^{-1} per year) the sample will allow quite detailed studies of this fermionic species. In the Minimal Standard Model (MSM) the top decays 100 % to a bottom quark and a W. Depending on the decays of the two W's present in the event, the $t\bar{t}$ event will consist of six jets (44 %); four jets, a high-momentum lepton and a neutrino (44 %); or two jets, two high-momentum leptons and two neutrinos (11 %). In all decays at least two b-flavored jets will be present. The total top quark width is given approximately by $\Gamma_t \sim 0.18\,\mathrm{GeV}(m_t/M_W)^3$: about 1.4 GeV for $m_t = 175\,\mathrm{GeV}$.

2.3.2.1 Detector Requirements for Top Physics

In $t\bar{t}$ physics the six jet final state is the hardest to reconstruct. Simulations were performed where the energy, momentum and angular resolutions of the detectable particles were varied. The granularity of a hadron calorimeter was also varied in the simulation. The resolution functions were parametrized as a sum of two Gaussian distributions in order to simulate deviations from simple Gaussian resolutions ($1\,\sigma + 5\,\sigma$). Previous studies [7, 8] have shown that of the currently available jet finding algorithms LUCLUS, which was used here, performs best. The performance of a hadron calorimeter was found to be of greatest importance, but a significant contribution to the resolutions of the reconstructed properties of the top quarks and the jets was found to be due to the jet finding algorithm.

2.3.2.2 Threshold Scan Studies

The large decay rate of the top quark carries as a consequence that toponia bound states do not form: this is the very first case in which E-Winteractions lead to a decay rate faster than the strong ones. The top width Γ_t acts as an effective cut-off energy for non-perturbative QCD effects. This facilitates the theoretical predictions, in particular, near the $t\bar{t}$ production threshold. An energy scan around the $t\bar{t}$ threshold will yield a very precise measurement of the top quark mass. Three observables can be used:

- The total production cross section $\sigma_{t\bar{t}}(s)$ which is particularly sensitive to m_t. This observable, however, is also quite sensitive to the strength of the $t\bar{t}$ binding potential.
- The top momentum distribution $d\sigma/dp(s)$ which again can be linked to the top mass and $\alpha_s(m_t)$.
- The forward-backward asymmetry $A_{FB}(s)$ which, due to the interference of S- and P-wave amplitudes, allows an independent although less sensitive evaluation of the top mass.

The cross section shape at threshold is distorted by initial state radiation effects (ISR) and energy smearing due to beamstrahlung (BS). The last effect is particularly important and leads to a smoother threshold behavior of the cross section. The results quoted in the following refer to beam energy spectra expected for the TESLA option: as one might anticipate both ISR and BS cause an effective loss of analyzing power toward the top mass measurement. The other two observables (momentum spectrum and forward backward asymmetry) are also affected although to a smaller extent. The threshold scan will only be effective for these studies if the spread of the beam momentum and the beamstrahlung are small and the detector is capable of making precise measurements of the luminosity spectrum, as has been discussed in the previous section. These three requirements are built into the machine and detector designs presented in this conceptual design report.

a) Event Selection

As mentioned before both the signal ($e^+e^- \to t\bar{t}$) and background ($e^+e^- \to Z\gamma$, $e^+e^- \to ZZ$, and $e^+e^- \to W^+W^-$) events were smeared according to the SIMDET algorithm. The smeared events were put through some selection and analysis as discussed below. For the $t\bar{t}$ cross section measurement events with six jets or four jet plus a prompt lepton were selected; in the six jets case the following requirements had to be satisfied:

- Thrust smaller than 0.85.
- Charged multiplicity greater than 20 ($p_t > 500\,\mathrm{MeV}/c$).
- Total reconstructed energy greater than 65 % $E_{\mathrm{c.m.}}$.
- At least six jets.

All the events which did satisfy these cuts were required to be reconstructed as six jets with the JADE algorithm. At this stage they were selected as top candidates if two W's were found within a bound of 30 GeV w.r.t the nominal W mass, the reconstructed top mass was within 60 GeV of its nominal value and at least one of the assumed b-jets was tagged as such. These requirements selected a sample of $t\bar{t}$ events with $\approx 23\,\%$ efficiency and a background contamination of $\approx 10\,\%$. The four-jet plus lepton sample was selected requiring that the JADE jet-finding algorithm found 5 jets; one of those had to contain a lepton with momentum greater than 20 GeV/c. The total energy of the *leptonic* jet should not exceed the lepton energy by more than 10 %. Top candidates were furthermore required to have a reconstructed W mass within 20 GeV of the nominal value, a reconstructed top mass within 50 GeV of the nominal value and, again, at least one of the assumed b-jets tagged as such. The overall efficiency came out to be 18.5 % while the remaining background in this sample was below 3 %. Events with one leptonic decay of the W were selected in a different way to measure the top momentum spectrum and charge asymmetry: in these events one of the top quark charge is unambiguously tagged by the leptonic decay of the W, the *other* top is momentum analyzed. The following criteria were used in this case, the purpose of which was to reduce backgrounds as much as possible. Briefly, the following additional requirements were imposed: a reconstructed total energy between 200 and 350 GeV, charged multiplicity below 5 in the *leptonic* jet and a total multiplicity of charged track and energy clusters smaller than 35 in the event, a positive anti-tag the two W-forming jets as b and reconstructing the W mass with those to better than 10 GeV were imposed. After this, 9.4 % of all top events were kept and no background remained. Assuming an integrated luminosity of $5\,\mathrm{fb}^{-1}$ per energy point, the top momentum was reconstructed with a resolution which ranged from about 30 % for the lowest energies to 18 % for the highest. The peak position of the top momentum distribution could be estimated with a relative precision ranging from $\Delta(p_{\mathrm{peak}})/p_{\mathrm{peak}} \simeq 12\,\%$ to 4 % as the machine energy is increased. Figure 2.3.1 shows how, in spite of the fact that detector effects do change appreciably the shape of the momentum distribution, its peak position remains quite stable. The probability of charge mislabelling, relevant for A_{FB}, has been found to be at the few per cent level. Figure 2.3.1 shows the top invariant mass as reconstructed after this selection. Table 2.3.1 summarizes the efficiencies and backgrounds obtained. These figures show a marked improvement with respect to the ones quoted in previous studies [9]: both better hardware performance and more sophisticated analyses are responsible for the overall upgrade in physics results.

b) Overall Energy Scan Results

The total cross section, the most probable top momentum and the forward-backward asymmetry are the three variables whose variation with center of mass energy, close to threshold, is most sensitive to the top mass. The most probable top momentum is the

Cross section measurement

	Efficiency	Background
6-jet	23 %	7 fb
4-jet	18.5 %	1.4 fb
TOTAL	41.4 %	8.4 fb

Top momentum measurement

	Efficiency	Background
4-jet	9.4 %	nihil

Table 2.3.1: *Summary of the selection efficiencies and background cross sections as obtained for $E = E_{\rm CM} - 2m_{\rm t} = 0$ with the analyses explained in the text.*

parameter which exhibit a smaller dependence on beam effects and uncertainties in the $\rm t\bar{t}$ binding potential with respect to the total cross section. The three observables are used in a χ^2-fit assuming a nine-point scan around $\sqrt{s} = 350\,\rm GeV$ with an integrated luminosity of $5\,\rm fb^{-1}$ per point[2]. An additional measurement below threshold is foreseen ($5\,\rm fb^{-1}$) to directly evaluate backgrounds. The fit has two free parameters: the top quark mass and $\alpha_s(M_Z^2)$, which appears in the QCD $\rm t\bar{t}$ potential. The results are shown in Fig. 2.3.2. The overall precision expected in the top quark mass and the strong coupling constant are:

$$\begin{aligned} \Delta m_{\rm t} &\leq 110\,\rm MeV \\ \Delta\alpha_s &\simeq 0.003 \end{aligned}$$

although their correlation is rather big. Most of the sensitivity comes from the total cross section measurement, (which alone leads to about $\Delta m_{\rm t} \simeq 140\,\rm MeV$ and $\Delta\alpha_s \simeq 0.0040$). Adding the constraint from the momentum distribution gives a significant improvement on the determination of $m_{\rm t}$ and helps to reduce the correlation with $\alpha_s(M_Z^2)$. The forward-backward asymmetry retains a much smaller analyzing power. The same data can be exploited to determine the top quark width. The forward-backward asymmetry does have some analyzing power for the width through the interference of the S- and P-wave amplitudes. Again a χ^2 fit to the same observables can be performed: the overall precision in the top quark total width will be around 18 %, once $m_{\rm t}$ and α_s are determined.

[2]This scan strategy has not been optimized. As a matter of fact, the cross section has the largest sensitivity to the top mass and α_s just at the rising edge of the $1S$ *peak*, about 2 to 3 GeV below the kinematical threshold. By concentrating the scan in that region, the results might improve by a fair amount.

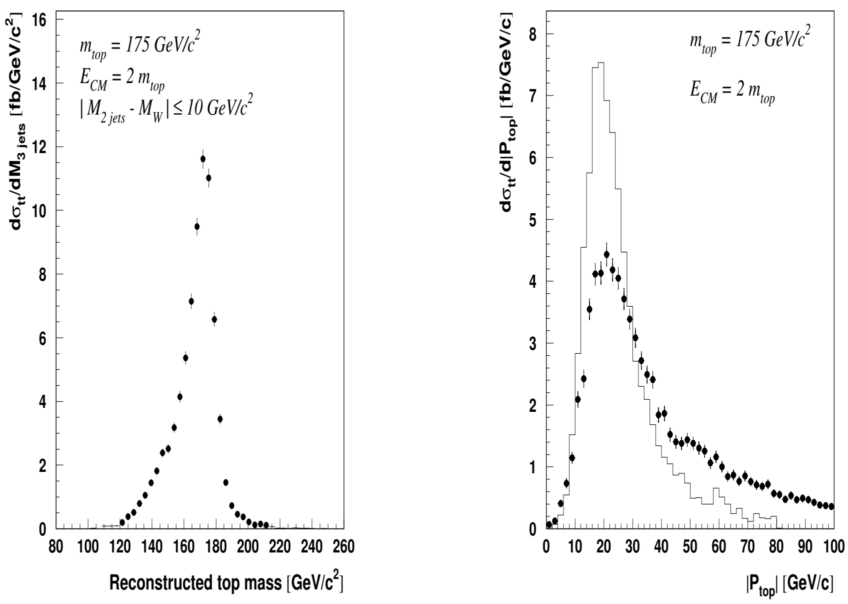

Figure 2.3.1: *The top invariant mass and the top momentum distribution as reconstructed with the 4-jet events selected for the momentum study. The solid line corresponds to the generated distribution.*

2.3.2.3 Other Measurements involving Top Quarks

Complete simulations involving other interesting measurements on top quarks physics, such as the study of top rare decays, the determination of the top form factors and its Yukawa coupling are in progress. Preliminary studies, however, carried out in previous workshops [10, 11, 12] indicate that the detector described in this chapter would cope with the demands that physics pose. There are also important possible effects of flavor violation in top quark processes (via the coupling $Z \to t\bar{c}$) which can be looked for very sensitively in the proposed detector, giving results which will complement those expected from the LHC [13]. To summarize this section, no limitation can be anticipated from the detector performance on the study of top quark physics. The results obtained show that, an e^+e^- collider running close to the top threshold can yield, with the proposed detector, a determination of the top mass better than 0.1 % and measure the strong coupling constant to better than 3 % accuracy.

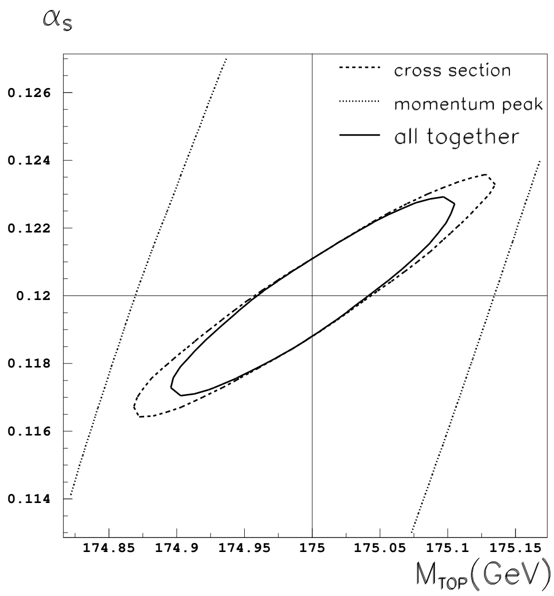

Figure 2.3.2: $1\,\sigma$ *contours in the top mass versus α_s plain which can be obtained with the measurement of the cross section and the top momentum distribution in a threshold scan.*

2.3.3 Higgs Physics

The discovery and study of Higgs bosons are among the primary goals for the very high energy program in particle physics. At an e^+e^- collider operating around half a TeV Higgs particles can be produced and studied in a completely unbiased way by means of the Z H associate production. This mechanism allows the absolute determination of the production cross section and, as a by product, the measurement of absolute branching ratios. Wherever a Higgs is first found, measurements of its decay branching ratios will be needed to confirm that it is indeed a Higgs particle and to identify which theory of electroweak symmetry breaking fits its properties. The measurement of the Higgs decay branching fractions to different fermionic species represents a crucial test of the Higgs sector in Standard Model (SM) [14]. A precise determination of the branching ratio for the decay $H \to b\bar{b}$ may allow to distinguish between the SM neutral Higgs boson H and its counterpart h^0 in the minimal supersymmetric SM extension (MSSM). Moreover, it has been suggested that the ratio of branching ratios $\frac{BR(H\to c\bar{c}+gg)}{BR(H\to b\bar{b})}$ may provide an evaluation of the CP-odd A boson mass, in the kinematical region not directly accessible in the first phase of operation of the e^+e^- linear collider [15].

In the following the results obtained for the search for a neutral Higgs boson, the determination of its production cross-section and of the branching ratios for its decays into hadronic final states are presented: simulations were run at two c.m. energies 360 GeV and 500 GeV. Z H events were generated with two different Higgs mass values of 120 GeV and 140 GeV. The signal $e^+e^- \to ZH$; $Z \to q\bar{q}$, $\ell^+\ell^-$, $\nu\bar{\nu}$ events and background (mainly Z Z) were generated using PYTHIA 5.702 and JETSET 7.405 tuned with the LEP data for the electroweak and QCD variables and with the CLEO and LEP data for the heavy flavor decays and including initial state radiation and beamstrahlung. The minimum luminosity necessary to obtain a statistical significance $S/\sqrt{B}$ greater than five on the Higgs signal at 360 GeV is compatible with what is required to carry out the top physics program. For the higher energy running, an integrated luminosity of $50\,\mathrm{fb}^{-1}$ is assumed in the error estimates for the branching ratios: this corresponds to about one year of running at the nominal luminosity.

The study of the Higgs boson production and decays requires good detector performances both in the energy/momentum determination and in the vertexing of charged tracks. Good resolution in the jet-jet invariant mass is needed, which in turn demands precise determination of the energy and the directions of the hadronic jets. Finally good momentum determination for high energy leptons from $Z \to \ell^+\ell^-$ is required in order to achieve good missing mass resolution. For adequate jet flavor tagging, stringent requirements for tracking and vertexing are to be met. From all of the above requirements it follows that precision study of the Higgs boson decays represent a hard challenge and set quite a number of benchmarks for the global performance of the detector.

The energies and momenta of generated particles which fall within the geometrical acceptance are smeared according to the expected detector resolutions. Tracking efficiency and impact parameter resolution are evaluated by using GEANT simulation of the silicon vertex tracker. Full pattern recognition, track refit, misassociation of vertex detector hits and background from the accelerator are included in the simulation in order to have a realistic assessment of tracking and vertex determination.

2.3.3.1 Higgs Observation and Determination of the $e^+e^- \to$ ZHCross Section

As it will be shown below, the Higgs signal at an e^+e^- machine can be observed already with a limited integrated luminosity provided that the Higgsstrahlung process holds ($\sqrt{s} \geq m_Z + m_H$). The cross section for this type of production can be determined with high accuracy without explicit assumptions on the Higgs decay modes. As already stressed before, this feature extends the sensitivity to non-standard types of Higgs bosons and reduces the experimental uncertainties in the determination of the Higgs decay branching ratios through the direct measurement of the Higgs production rate.

To measure the $e^+e^- \to ZH$ cross section σ_{ZH}, inclusive of all decay channels, the main technique consists in selecting events with two isolated fast charged particles consistent with $Z \to \ell^+\ell^-$ and then computing the mass recoiling against them. This

Reaction	Luminosity needed (fb^{-1})	
	Recoil Mass Technique	Invariant Mass Technique
$e^+e^- \rightarrow \ell^+\ell^- q\bar{q}$	10	10
$e^+e^- \rightarrow \nu\bar{\nu} q\bar{q}$	–	1
$e^+e^- \rightarrow \tau\bar{\tau} q\bar{q}$	80	80
$e^+e^- \rightarrow 2q2\bar{q}$	3	3
$e^+e^- \rightarrow 3q3\bar{q}$	50	50

Table 2.3.2: *Integrated luminosity required to observe an* H *signal with* $S/\sqrt{B} \sim 5$ *or better. The* H *mass is assumed to be* 140 GeV *and* $\sqrt{s} = 360$ GeV.

technique has already been used in previous analyses [17]. Here, the guidelines of these for the reconstruction method were used, while the selection criteria have been improved and further constraints were explicitly imposed, when appropriate, in order to achieve better experimental resolution [18]. For instance, a beam constraint fit on the particle tracks was performed in order to obtain the best possible momentum resolution and furthermore the resulting missing mass was reevaluated by forcing the candidate lepton pair to the Z mass.

Figure 2.3.3 shows the result for a Higgs boson mass of 140 GeV with $\sqrt{s} = 360$ GeV and an integrated luminosity of 50 pb^{-1}. The signal is clearly visible over the background which is dominated by $e^+e^- \rightarrow ZZ$ with $Z \rightarrow \ell^+\ell^-$. The irreducible background for the $H \rightarrow W^+W^-$ channel, for which no Monte Carlo event generator exists, has been estimated to be small and has been neglected. The cross-section σ_{ZH} is measured to a precision of $\sim 6\,\%$, for this Higgs boson mass where the $H \rightarrow b\bar{b}$ rate is roughly equal to the $H \rightarrow W^+W^-$ one. A similar analysis for a 120 GeV Higgs mass, where $H \rightarrow b\bar{b}$ dominates, gives a precision on σ_{ZH} of $\sim 5\,\%$.

To measure the branching ratios of the Higgs boson it is necessary to split up the cross section σ_{ZH} into its topological subchannels. In each channel a search is made for the Higgs boson peak above background, either in the directly measured invariant mass of the Higgs boson decay products or in the recoil mass distribution, calculated as for Fig. 2.3.3. Table 2.3.2 shows the result for a Higgs boson mass of 140 GeV in terms of the integrated luminosity required at $\sqrt{s} = 360$ GeV to observe the peak in each topology with a significance of $S/\sqrt{B} \sim 5$ or better. In the table for each listed 4-body final state, all diagrams at tree level have been considered. In particular, the $\tau^+\tau^-\, q\bar{q}$ final state involves also the $H \rightarrow \tau^+\tau^-$ contribution. For some of these final states, like for instance $\nu\bar{\nu}\, q\bar{q}$, other production mechanisms like the WW fusion, do

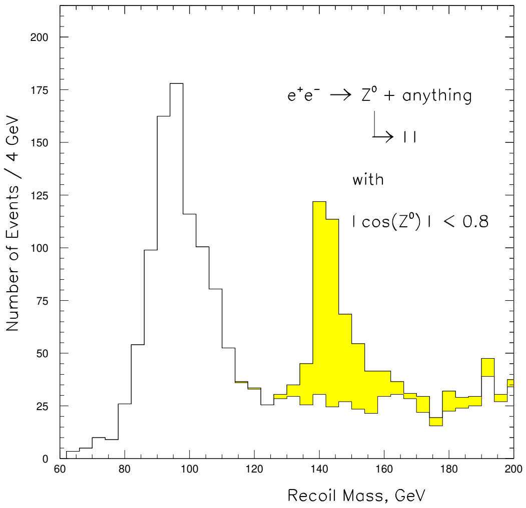

Figure 2.3.3: *The dilepton recoil mass distribution showing the signal of a* 140 GeV *Higgs boson produced together with the* Z *at* $\sqrt{s}$ = 360 GeV *for an integrated luminosity of* 50 fb^{-1}.

play a relevant rôle and hence, the resulting luminosity does not follow the simple Z branching ratio expectation.

2.3.3.2 Measuring Higgs Hadronic Decay Branching Ratios

The accuracy with which a given Higgs decay branching fraction can be measured depends on the experimental capability of identifying the different fermionic species in the decay. Since the decay $\mathrm{H} \to \mathrm{b\bar{b}}$ is the dominant decay mode for Higgs masses up to about 130 GeV, an efficient b-tagging capability is a prerequisite of this analysis. Moreover, the large $\mathrm{b\bar{b}}$ yield requires also efficient anti-b tagging in order to reject b jets in the study of the Higgs boson decays into lighter quark or gluon pairs. For the measurement of the Higgs decay branching ratios, Higgs decays to hadronic final states are reconstructed using both four jet ($jjjj$), two jet and two lepton ($jj\ell\ell$), and two jet plus missing energy ($jj\nu\nu$) topologies in the process $\mathrm{e^+e^-} \to \mathrm{HZ}$. The details of the selection criteria applied can be found in [19]. After the jet clustering, the energies of the reconstructed jets are rescaled imposing energy and momentum conservation at $\sqrt{s}$. Then the jets are paired and a final cut is applied, imposing compatibility with the $\mathrm{e^+e^-} \to \mathrm{ZH}$ hypothesis using the reconstructed jet-jet masses. The selection efficiency for $\mathrm{e^+e^-} \to \mathrm{ZH}$, $\mathrm{Z} \to$ anything, $\mathrm{H} \to \mathrm{q\bar{q}}$ and gg are summarized in Tab. 2.3.3 for two values of the $\sqrt{s}$ energy and of the Higgs boson mass m_{H}. To measure the branching ratios BR(H $\to$ b$\bar{\mathrm{b}}$) and BR(H $\to$ c$\bar{\mathrm{c}}$ + gg), the quark content of the di-jet system originating from the Higgs decay needs to be tagged. Methods of quark flavour tagging at e^+e^- colliders have been developed and successfully applied at LEP and SLC to study the hadronic decays of the Z boson. At a high energy linear collider, these

$\sqrt{s}$ (GeV)	360	360	500	500
m_{H} (GeV)	120	140	120	140
H Z Efficiency	22 %	20 %	26 %	24 %

Table 2.3.3: *The efficiency obtained for the reconstruction of the* $e^+e^- \to$ ZH*; Z* $\to$ *anything,* H $\to$ q$\bar{\mathrm{q}}$, gg.

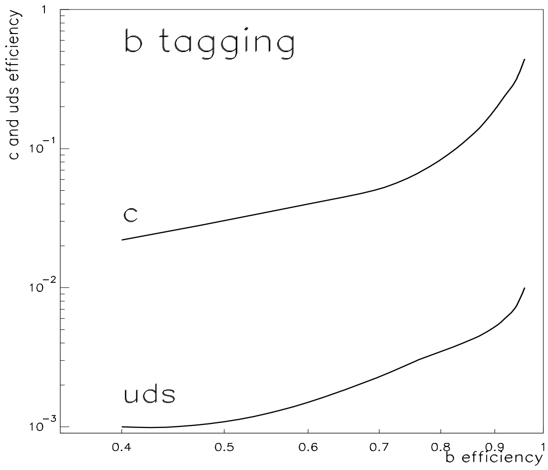

Figure 2.3.4: *The probability of classifying a* c$\bar{\mathrm{c}}$ *(upper curve) or a lighter* q$\bar{\mathrm{q}}$ *pair (lower curve) as* b$\bar{\mathrm{b}}$ *plotted as a function of the efficiency of tagging* b$\bar{\mathrm{b}}$ *pairs from Higgs decays.*

techniques can be further improved by exploiting the favourable kinematics and the performance of an optimized detector for tagging heavy quarks. In particular the large boost to the short-lived (b and/or c) hadrons and the extremely good tracking accuracy, which the silicon vertex tracker will provide, allows the use of inclusive algorithms for the identification of their decays. In the present analysis the impact parameters of both tracks and the invariant mass of the candidate decay products have been used to distinguish b's from non-b hadronic jets. Briefly, the impact parameter tagging tests the compatibility of the charged tracks in a jet to be originating from a common primary vertex, comparing their impact parameters with the estimated impact parameter error, which includes multiple scattering and the position and width of the luminous spot, which in a linear collider is extremely small and very well defined $\mathcal{O}(10\,\mu\mathrm{m})$. Due to the relatively long decay distances of beauty and charm hadrons, the probability distribution for this hypothesis exhibits a sharp peak at zero (b and c jets); u, d and s jets generate a flat spectrum between 0 and 1. In addition, b jets are characterised by the relatively high mass of the decaying b hadrons. An inclusive algorithm is used to select the candidate products of b and c decays in a jet and to estimate the invariant mass of the secondary particles jet by accounting for the invariant mass of the selected particles, their energy, the jet energy and the b quark fragmentation function. The various kinematic quantities computed for each jet are combined for the di-jet system representing the candidate H decay once that the jets are b- (or anti b)-tagged.

The performance of the $\mathrm{b\bar{b}}$ tagging algorithm is shown in Fig. 2.3.4 where the probability for a $\mathrm{c\bar{c}}$ and a light $\mathrm{q\bar{q}}$ pair to be tagged as $\mathrm{b\bar{b}}$ is plotted as a function of the efficiency for identifying a genuine $\mathrm{b\bar{b}}$ di-jet from the Higgs decay for different tagging criteria. The use of the jet mass algorithm provides an efficient mean of reducing the charm contamination in the b-tagged sample while retaining a significant efficiency for $\mathrm{H} \to \mathrm{c\bar{c}}$ decays with an anti-tag against b quarks. As a matter of fact, the reconstruction of the non-$\mathrm{b\bar{b}}$ decays of the Higgs is affected by a significantly larger background as compared to the $\mathrm{b\bar{b}}$ channel. Since the main interest of the study of these decays is the determination of the ratio $\frac{\mathrm{BR(H\to c\bar{c}+gg)}}{\mathrm{BR(H\to b\bar{b})}}$, events with an anti-tag against b quarks are used for the measurement of non-$\mathrm{b\bar{b}}$ hadronic Higgs decays without attempting to separate $\mathrm{c\bar{c}}$ from the other modes. The background contribution to each candidate sample is estimated from the simulated background events and from the misassignemet probability for genuine Higgs decays and subtracted. By combining the $jjjj$ and $jj\ell\ell$ with the $jj\nu\nu$ channels an experimental accuracy on the measurement of $\sigma_{\mathrm{ZH}}\mathrm{BR(H \to b\bar{b})}$ of better than 4.0 % can be obtained for a Higgs mass of 120 GeV at both 360 GeV and 500 GeV centre-of-mass energy. The ratio $\frac{\mathrm{BR(H\to c\bar{c}+gg)}}{\mathrm{BR(H\to b\bar{b})}}$ can be determined with an accuracy of 20 % for $m_{\mathrm{H}} = 120\,\mathrm{GeV}$, or about 50 % if $m_{\mathrm{H}} = 140\,\mathrm{GeV}$ (see Tab. 2.3.4). The above figures should be compared with the theoretical uncertainties on the same quantities, about 3 % for the $\mathrm{b\bar{b}}$ mode and 11 % for $\mathrm{c\bar{c}}$ plus gg, due to less than perfect knowledge of α_s and the quark masses.

The significance of these results in the study of the properties of a neutral Higgs boson is exemplified by defining the region of the m_{H}, $\tan\beta$ plane where the MSSM h^0 boson can be distinguished from the SM Higgs boson. It is assumed, in the following, $M_{\mathrm{SUSY}} = 1\,\mathrm{TeV}$, $m_{\mathrm{t}} = 180\,\mathrm{GeV}$ and maximal squark mixing. A comparison of the ratio $\frac{\mathrm{BR(H^0_{SM}\to b\bar{b})-BR(h^0_{MSSM}\to b\bar{b})}}{\mathrm{BR(H^0_{SM}\to b\bar{b})}}$ with the fractional error on the absolute branching ratio $\mathrm{BR(H \to b\bar{b})}$ measured from the total Higgsstrahlung cross section and the $\sigma \times \mathrm{BR}$

m_{H} (GeV)	120	140
$\Delta(\sigma_{\mathrm{ZH}}\,\mathrm{BR}(\mathrm{H}\to\mathrm{bb}))$	3.8 %	6.2 %
$\Delta(\sigma_{\mathrm{ZH}}\,\mathrm{BR}(\mathrm{H}\to\mathrm{c\bar{c}},\mathrm{gg}))$	19 %	47 %
$\Delta(\frac{\mathrm{BR}(H\to\mathrm{c\bar{c}},\mathrm{gg})}{\mathrm{BR}(\mathrm{H}\to\mathrm{bb})})$	20 %	48 %

Table 2.3.4: *Relative accuracy Δ on the determination of the branching ratios for the Higgs hadronic decay modes. The experimental accuracy corresponds to an integrated luminosity of* $50\,\mathrm{fb}^{-1}$ *at either* $\sqrt{s} = 360\,\mathrm{GeV}$ *or* $500\,\mathrm{GeV}$.

for the bb channel allows a discrimination between the SM Higgs and the MSSM one. Experimental errors are obtained combining two data sets, at 360 GeV and 500 GeV ($50\,\mathrm{fb}^{-1}$ each). The theoretical uncertainty is also taken into account and convoluted with experimental errors. Figure 2.3.5 shows the region in which the SM and MSSM hypotheses can be distinguished at the 90 % confidence level. The constraints from the theoretical upper bound on the h^0 mass in the MSSM including radiative corrections and the expected exclusion region from the LEP 2 data at $\sqrt{s} = 192\,\mathrm{GeV}$ are folded in. The results from the $\mathrm{b\bar{b}}$ branching ratio measurement cover most of the region of the plane; the area left uncovered is minimal. A high energy $\mathrm{e^+e^-}$ collider will yield an uncontroversial assessment of the H^0 nature.

2.3.4 Production of the HA Final State

A typical final state which can be expected in the MSSM is the associated production of H and A Higgs bosons. This process has been simulated in detail with the goal of determining the precision on the mass and production cross section the linear collider would yield, in a direct measurement. The following sets of MSSM parameters were assumed for the analysis:

$$M_{\mathrm{A}} = 260 \text{ or } 300 \text{ or } 340 \text{ GeV}$$

with

$$\begin{aligned} \tan\beta &= 50 \\ \mu &= 551\,\mathrm{GeV} \\ M_2 &= 185\,\mathrm{GeV} \end{aligned}$$

In such a scenario the lowest lying Higgs boson h will have a mass of $\approx 110\,\mathrm{GeV}$ and would be almost standard model like. The associate production h A and Z H will be suppressed, therefore direct evidence of the MSSM Higgs sector can be achieved

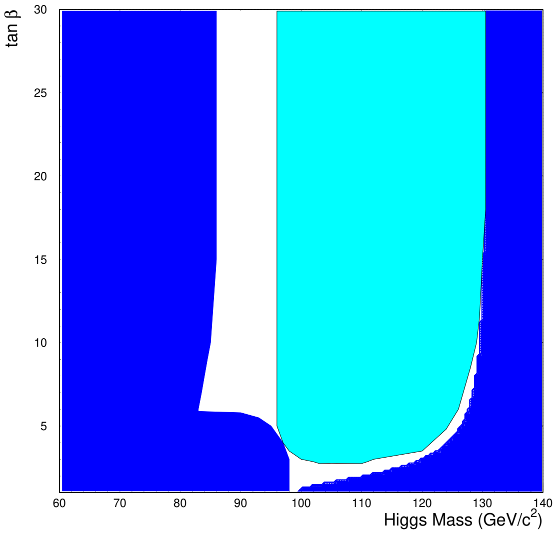

Figure 2.3.5: *The region of the* $m_{\rm H}$, $\tan\beta$ *plane where the MSSM neutral Higgs boson* $\rm h^0$ *can be distinguished from the SM boson* H *(gray area). This plot has been obtained for* $m_{\rm t} = 180\,\rm GeV$, $M_{\rm SUSY} = 1\,\rm TeV$ *and maximal squark mixing. The LEP 2 expected exclusion region is shown in dark at the left. The constraint from the theoretical upper bound on the* $\rm h^0$ *mass in the MSSM including radiative corrections is shown in dark at the right.*

studying this particular final state. With the parameters listed above H and A have similar masses, branching ratios ($\rm b\bar{b} \approx 90\,\%, \tau^+\tau^- \approx 10\,\%$) and widths ($\approx 15\,\rm GeV$). The mass range was chosen in order to be above the threshold of A and H production at $\sqrt{s} = 500\,\rm GeV$ and below the threshold for the decay $\rm A/H \to t\bar{t}$. The cross section is expected to be 7.8, 5.6 and 2.4 fb respectively for the three mass hypotheses. An integrated luminosity of $\mathcal{L} = 200\,\rm fb^{-1}$ at $\sqrt{s} = 800\,\rm GeV$ was assumed.

2.3.4.1 Simulation and Event Selection

6000 $\rm e^+e^- \to HA$ events at each mass value (i.e. between four and twelve times the expected amount of data) were generated using the HZHA code [20]. Signal events produce final states with four jets, so that standard processes expected to contribute to the four-jet topology as background sources are:

- $\rm e^+e^- \to \gamma/Z \to f\bar{f}$
  $\rm f\bar{f}$ s channel production via γ/Z was generated using PYTHIA [7]. After the

selection, the only surviving events in this sample were the $t\bar{t}$ ones and, to get better statistical significance, a special set of these events were generated with JETSET.

- $e^+e^- \to ZZ/WW \to f\bar{f}\,f\bar{f}$ and $e^+e^- \to f\bar{f}\,f\bar{f}$
  4-fermion events were generated using PYTHIA with double vector boson production and EXCALIBUR [21]. The two generators were found to be compatible. The only relevant background was found to come from $e^+e^- \to b\bar{b}\,b\bar{b}$, $e^+e^- \to b\bar{b}\,c\bar{c}$, and $e^+e^- \to cscs$ for which special samples were generated.

The generated events were processed through the SIMDET code to add detector effects in the event reconstruction. All particles with energy greater than 1 GeV and $|\cos\theta| < 0.95$ were used as input for the jet reconstruction algorithm. The reconstructed particles were clustered into four jets according to the JADE algorithm. Jets with at least 5 charged particles were classified as *hadronic* and jets with 1 or 3 charged particles and an invariant mass lower than 3 GeV as *leptonic*. Only topologies with 4 hadronic jets (corresponding to 4b-decays) or 2 hadronic and 2 leptonic jets (corresponding to $bb\tau\tau$ decays) were initially considered. The energies of the four jets were afterward rescaled imposing the total energy-momentum conservation with the assumption that the four jet velocities $\bar{\beta}_i = \bar{p}_i/E_i$ were measured correctly. Compatibility of the events with the four body hypothesis was enforced requiring all the recomputed energies be positive. The requirements of positive energies after rescaling, and of a four-jet topology, were effective in reducing background coming from channels which did not have just four hard jets, such as $e^+e^- \to t\bar{t}$ (6 jets or 4 jets plus a prompt lepton) or $e^+e^- \to q\bar{q}\,gg$ (2 leading jets and two soft gluon jets) and yielded a reasonably high ($\approx 60\,\%$) efficiency for the $e^+e^- \to HA$ signal. After the kinematical fit, jets were paired and di-jet invariant masses were computed from the rescaled energies. To reject $e^+e^- \to ZZ/WW \to f\bar{f}\,f\bar{f}$ background, events with at least one di-jet combination with both di-jet masses lower than 120 GeV were discarded. $t\bar{t}$ contamination was further reduced rejecting events with at least one di-jet combination with distance from the point (m_t, m_t) lower than 50 GeV. At this stage of the analysis, since the 2 hadronic and 2 leptonic jets sample had a relevant background from $e^+e^- \to q\bar{q}\,gg$ events, with gluon jets having low multiplicity and low invariant mass, only topologies with 4 hadronic jets were further considered. A b-tagging algorithm based on lifetime probability tag [22, 23, 24] was then performed, using two dimensional track impact parameter significance. As the most important background was found to be $t\bar{t}$ production, which contains always two (and only two) b jets, the sum of the two highest jet probabilities was used as discriminating variable, requiring also all the four jets to have a significant probability to come from a b quark. A summary of the selection criteria is displayed in Tab. 2.3.5 for the signal and for the surviving backgrounds, $t\bar{t}$, $b\bar{b}\,b\bar{b}$, and $b\bar{b}\,c\bar{c}$ only. The $f\bar{f}$ sample included also the $t\bar{t}$ which yielded the only two fermions

	HA (260, 300, 340 GeV)	$t\bar{t}$	4b	2b2c
Cross section [fb]	7.8, 5.6, 2.4	280	6.2	12.5
Generated events	6000, 6000, 6000	30000	5000	5000
4 hadronic jets	.81	.49	.22	.21
Kinematic fit	.61	.36	.15	.15
WW,ZZ rejection	.61	.36	.05	.08
m_t compatibility	.59	.20	.04	.07
b-tagging	.21	.001	.01	.002

Table 2.3.5: *Summary of the generated events (signal and background) and their selection efficiencies at the various stages of the selection.*

surviving events. Out of the cscs sample, no event survived the selection criteria, giving us confidence on the goodness of the method. An efficiency of 21 %, with a purity of 69 % was obtained for $m_A = 300\,\text{GeV}$. This figure can be substantially improved without a significant loss of efficiency if a cut on the di-jet invariant masses is applied (this technique is discussed in the next section). More details about this selection can be found in [25].

2.3.4.2 Masses and Cross Section Determinations

The A and H masses can be measured exploiting the fact that, in the scenario discussed, they are almost mass-degenerate, therefore only one mass need to be determined. From the selected event sample a dijet invariant mass distribution was formed, choosing the combination with minimal difference between the two masses and discarding the combination in which the two most energetic jets were paired together. The distribution obtained (Fig. 2.3.6), shows a mass peak with a width of 15 GeV; such width comes mostly from hadronization effects. With a calorimeter segmentation two times worse than the one proposed (in this case the energy flow algorithm was less effective) the mass resolution was $\approx$ 20 % worse. Once a peak is established in the di-jet mass distribution (or if the mass is already known by other means, e.g. LHC), it is also possible to reduce the number of wrong pairings, choosing the di-jet mass combination with better compatibility to the central value of the peak (Fig. 2.3.7). The overall error on the H and A bosons masses, using this technique, comes out to be 1.5 GeV, approximately independent of the mass. By the same token, the purity of the event sample can be improved to obtain a more precise measurement of the production cross section, selecting the di-jet combinations. For instance, a minimum invariant mass requirement of 200 GeV would yield a sample with an efficiency and purity of 20 % and

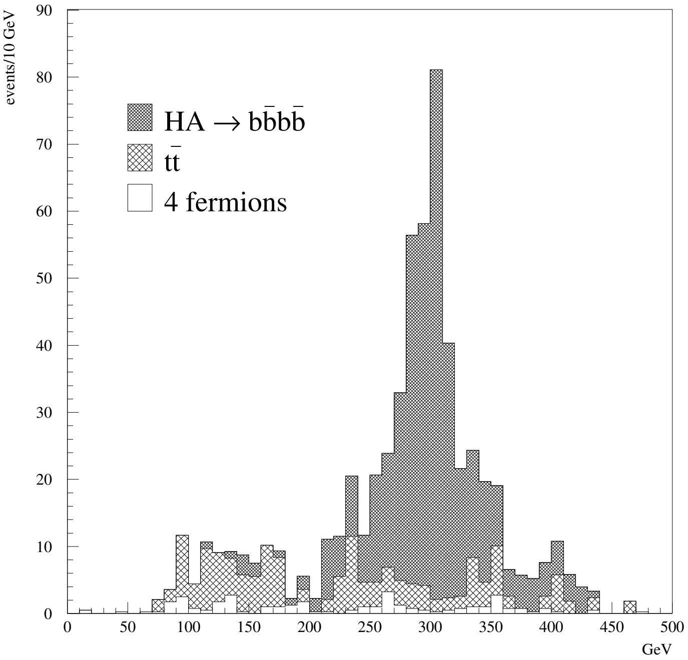

Figure 2.3.6: *Distribution of the di-jet invariant mass for the jet pair combination with the smallest mass difference.*

80 % respectively. This, in turn, allows a determination of $\sigma(e^+e^- \to HA) \times BR(A \to bb) \times BR(H \to bb)$ with a relative accuracy of 7 %, for $m_{A,H} = 300\,GeV$. The same technique was applied to the other masses and was found to provide accuracies on $\sigma(e^+e^- \to HA) \times BR(A \to bb) \times BR(H \to bb)$ of 5 % and 11 % for $m_{A,H} = 260$ and 340 GeV respectively. In conclusion, the reaction $e^+e^- \to HA$ can be isolated and studied in detail without any experimental limitation coming from the proposed detector. With simple selection criteria a clean event sample can be obtained with a manageably small background. The b-tagging performance of the proposed detector is essential in selecting an event sample which can be used to give precise measurements of both the mass and the cross section. For a luminosity of $\mathcal{L} = 200\,fb^{-1}$ at $\sqrt{s} = 800\,GeV$ the expected statistical accuracy is:

$$\Delta m_{A,H} \approx 1.5\,GeV,$$

$$\Delta\sigma(e^+e^- \to HA) \times BR(A \to bb) \times BR(H \to bb) \approx 5 - 11\,\%.$$

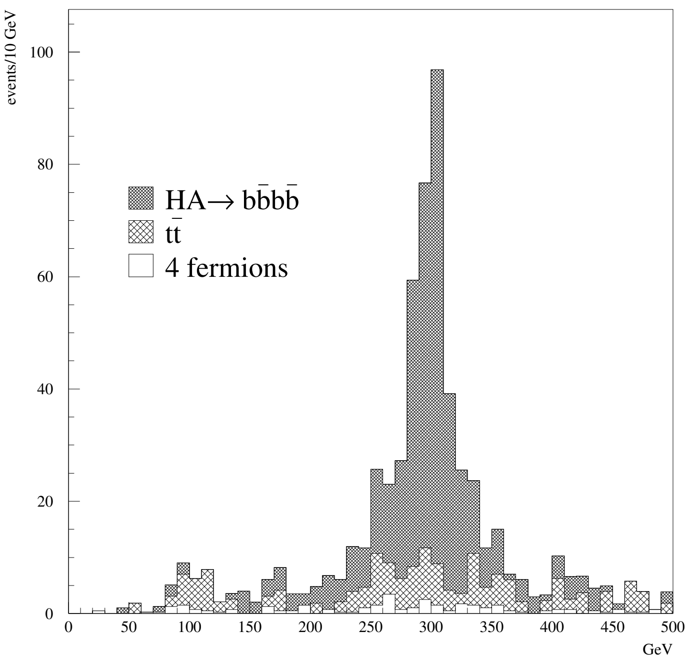

Figure 2.3.7: *Distribution of the di-jet invariant mass for the jet pair combination with better compatibility to the central value of the peak.*

Even with a reduced integrated luminosity of $\mathcal{L} = 50\,\mathrm{fb}^{-1}$, the signal to background ratio $S/\sqrt{B}$ is still ≈ 10 for the more unfavorable case of $m_{\mathrm{A,H}} = 340\,\mathrm{GeV}$ (expected cross section 2.4 fb), thus making this type of reaction clearly detectable by the combination of the proposed machine/experimental apparatus.

2.3.5 $\mathrm{e^+e^-} \to \mathrm{WW}$

W-pair production in $\mathrm{e^+e^-}$ annihilation is described at the lowest order in the Standard Model by three diagrams: two in the s channel containing the triple gauge boson couplings and one in the t channel with ν_e exchange; the latter gets contributions from left-handed electrons only. Different generators are available to simulate this process: at first, the compatibility of various codes with the Born approximation of CompHEP [26] has been checked. In Fig. 2.3.8 the CompHEP result is presented as a full line. In the same plot the results of different generators ([27],[28],[29],[21]) at $\sqrt{s} = 360$, 375, 500, 800 and 1600 GeV are shown.

variable	cut num.	value (e sel.)	eff.	cut num.	value (μ sel.)	eff.
$\cos\theta_l$	1	$\leq$ 0.9848+lumi	0.91	1	≤ 0.95	0.60
p_l	2	$\geq 20\,\mathrm{GeV}$	0.90	2	$\geq 20\,\mathrm{GeV}$	0.56
α_{iso}	3	$\geq 23°$	0.87	3	$\geq 30°$	0.55
E_{had}	4	$\geq 0.2 * \sqrt{s}$	0.77			
M(lmiss)	5	50 - 110 GeV	0.54	5	60 - 100 GeV	0.46
M(jj)	6	60 - 100 GeV	0.48	6	60 - 100 GeV	0.45

Table 2.3.6: *Selection cuts as used in the* WW *analysis.*

All cross-sections were calculated for resonant W diagrams without beamstrahlung or initial state radiation (ISR) and without any selection or cuts. All cross-sections agree within few percent. Once the initial state radiation and beamstrahlung effects are included, the total cross section is $\approx 8\,\mathrm{pb}$ at 500 GeV. An event sample of $50\,\mathrm{fb}^{-1}$ luminosity will contain 400 k WW-pairs. To determine triple gauge boson couplings from WW events in e^+e^- annihilation, the charge of the W has to be identified. This is readily done by measuring the charge of the daughter-lepton. The leptonic branching ratio for the W ($W^- \to e^-\nu$ and $W^- \to \mu^-\nu$) will then give about 40 k events of each type.

2.3.5.1 Generation of W Pairs and Background Reactions

W pairs were generated with two different generators ERATO [27] and WOPPER [28]: in both cases the couplings were set to the Standard Model values. Initial state radiation and beamstrahlung were simulated through the CIRCE code [30] in its TESLA implementation.

The detection efficiency is essentially dependent on the polar angle of the produced lepton (θ_l or $\cos\theta_l$).

About 30 k WW-pairs decaying to $\mu^\pm\nu q\bar{q}$ were generated for resonant W diagrams using the ERATO code; approximately the same number of W pairs decaying each into electron and muon final states were generated from resonant and non-resonant W diagrams using the WOPPER code.

Table 2.3.6 summarizes selection cuts and efficiencies for the two lepton species. In this simulation, the muon coverage includes only the tracking solid angle while electrons are assumed to be detected and identified also in the calorimeters (including the luminosity monitor). The isolation criteria for muons require the closest jet to be 30° away from the lepton. For electrons, the requirement is having a jet energy of less than 10 GeV in a cone of 23° centered in the lepton track. The selection efficiency for the electron final states is 0.480 ± 0.003, for muons 0.450 ± 0.003.

In the present analysis background events can be split in two classes: background

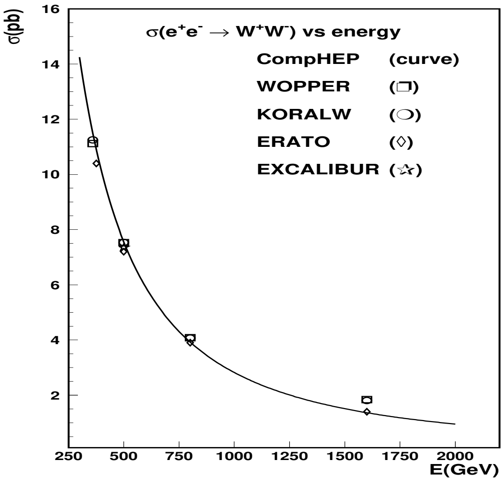

Figure 2.3.8: *Total cross-section of* WW *pair production.*

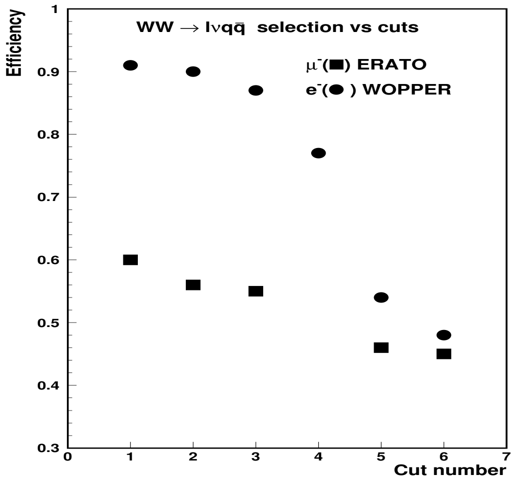

Figure 2.3.9: *Selection efficiencies as a function of the selection cuts.*

from the other W decay and background from processes which do not involve primary W's (e.g. $e^+e^- \rightarrow ZZ, t\bar{t}, q\bar{q}$). All these processes were generated at 500 GeV using PYTHIA [7], including ISR and beamstrahlung. The background contamination for the various sources is summarized in Tab. 2.3.7. The selected sample purity is high: only 2.24 % background contamination is allowed in.

2.3.5.2 Experimental Resolutions

The resolution on the lepton momenta as a function of momentum and as a function of $\cos\theta_l$ is shown in Fig. 2.3.10. A minimum momentum 20 GeV/c was required to cut-out leptons coming from semileptonic decays of heavy quarks.

The expected momentum resolution for selected leptons is $\approx 2\,\%$. The above figure applies to the entire inner tracker coverage ($|\cos\theta_l| \leq 0.83$), so that no charge mislabelling is expected for these events.

Selected events were then forced to have two jets according to the Durham algorithm [31]. A kinematical fit was performed after the event selection requiring four-momentum conservation and equal masses of the two W bosons. The W invariant mass reconstructed from the hadronic decay is the one which is better determined.

Figure 2.3.12 shows the mass plots for the invariant jet-jet mass for the electron and Fig. 2.3.13 for the muon final state.

Reaction $e^+e^- \to$	cross-section pb	events after cuts	rate %
$WW \to q\bar{q}\,q\bar{q}$	3.6	–	–
$\ell\nu\,\ell\nu$	0.8	–	–
$\tau^-\nu\,q\bar{q}$	0.6	260	1.8
$q\bar{q}$	12.0	3	0.02
$t\bar{t}$	0.6	3	0.02
ZZ	0.4	50	0.4
all			2.24

Table 2.3.7: *Background contributions to* $e^+e^- \to W^+W^- \to \ell\nu q\bar{q}$ *events from the different reactions, corresponding to the integrated luminosity of* $50\,\mathrm{fb}^{-1}$.

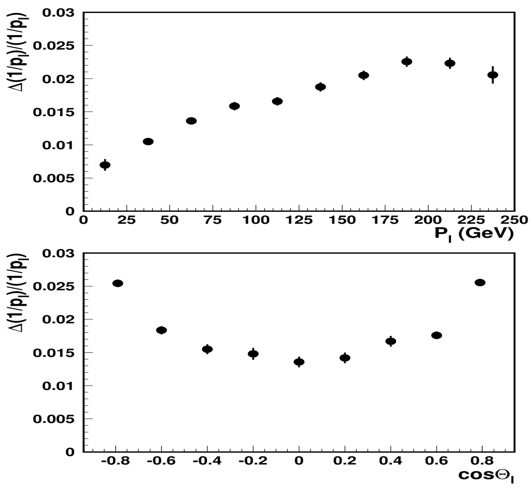

Figure 2.3.10: *Lepton momentum resolution as a function of the momentum (upper plot) and* $\cos\theta_l$ *(lower plot).*

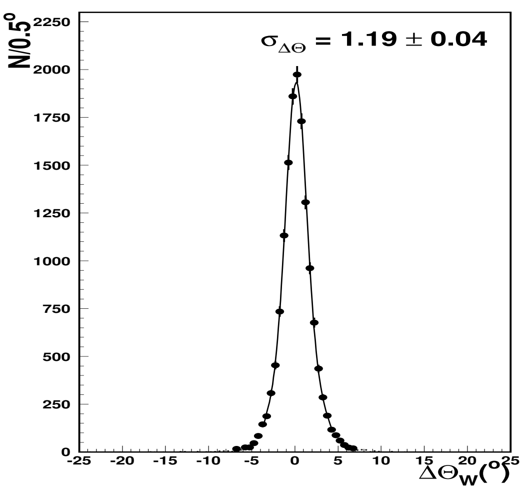

Figure 2.3.11: *Angular resolutions for* θ_W *as reconstructed from the two jets.*

The invariant mass distributions obtained, have been fit with a convolution of a Breit-Wigner and a Gaussian according to:

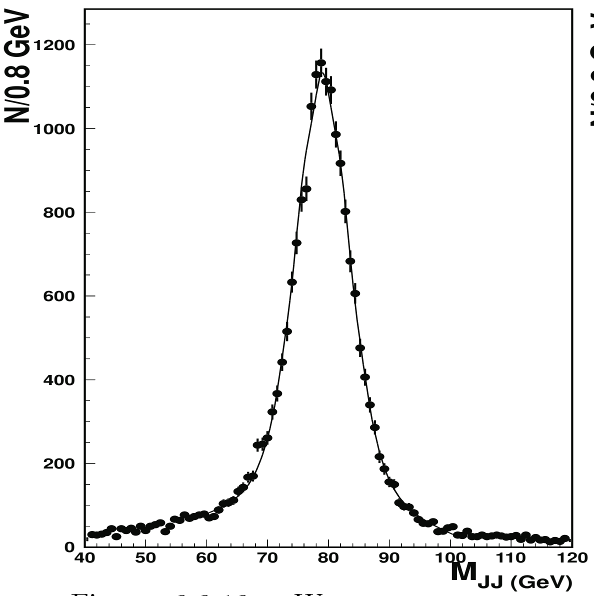

Figure 2.3.12: W *mass spectrum from invariant jet-jet mass for the electron final state.*

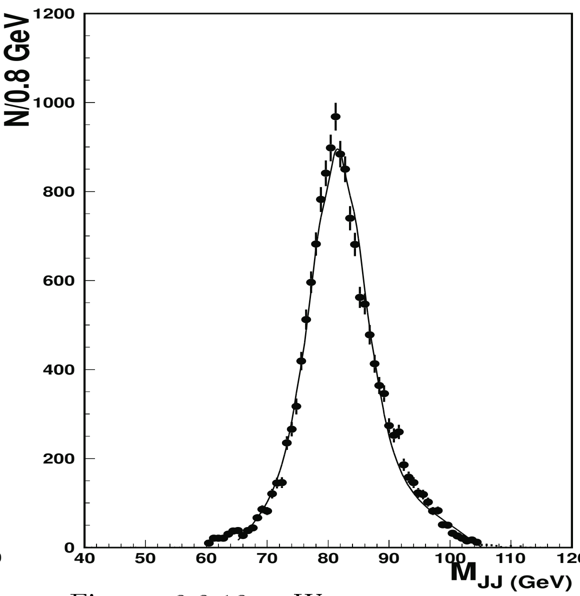

Figure 2.3.13: W *mass spectrum from invariant jet-jet mass for the muon final state.*

$$N(m, m_{\mathrm{W}}, \Gamma_{\mathrm{W}}, \sigma) \quad = \quad \int_{y_1}^{y_2} BW(y; m_{\mathrm{W}}, \Gamma_{\mathrm{W}}) G(y - m, \sigma) dy. \qquad (2.3.2)$$

The width of the Breit-Wigner was chosen to be the width of the W in the Monte Carlo generator. The width of the Gaussian parameterizes detector effects. The fitting procedure resulted in an experimental width of 3.6 GeV for electron and muon final states. The integration limits were set at four σ's.

A systematic shift of the fitted mass toward lower than the nominal value was observed in the case of hadronic decays. This effect can be explained as wrong assignments of particles inside a jet, loss of some jet-energy outside of the acceptance of the detector and detector thresholds; a correction on a statistical basis can be applied to the data a posteriori.

The best accuracy one might envisage on m_{W} is given by the distribution width scaled by $\frac{1}{\sqrt{N}}$, N being the total number of W's in the mass plot. Taking into account all semileptonic final states and their efficiency a statistical error of ≈ 15 MeV can be expected for 50 fb^{-1}. Systematics however, set in before the statistical limit is reached. A preliminary investigation of systematic effects results in an expected error of 15 MeV leading to 20 MeV on the W mass. More sophisticated analyses of the systematics are in progress; some improvement could come from these. The resolutions on θ_{W}, $\cos\theta_l$,

resolution of	μ sel.	e sel.
$\cos\Theta_{\mathrm{W}}$	0.0083	0.0082
Θ_{W}	1.20	1.19
$\cos\Theta_q$	0.026	0.027
Θ_q	2.5	2.6
ϕ_q	3.0	2.8
$\cos\Theta_l$	0.050	0.067
Θ_l	2.7	2.6
ϕ_l	4.0	3.9

Table 2.3.8: *Resolutions for* W *production angle and its decay products angles in the* W *rest frame (the angles are measured in degrees).*

and ϕ_l as well as $\cos\theta_q$ and ϕ_q play an important role in the determination of the anomalous couplings. Table 2.3.8 summarizes the results of the simulations.

2.3.5.3 Limits on the Anomalous Couplings

A maximum likelihood fit has been used to evaluate the sensitivity to measure anomalous couplings. The matrix element M_i for each event was calculated with the ERATO generator using the 4-momenta of the lepton, neutrino and two jets after the constrained fit. The minimization function is given by:

$$-\log \prod_{i=1}^{N_{\mathrm{events}}} \frac{|M_i|^2}{\sigma_{\mathrm{tot}}}. \tag{2.3.3}$$

The fact that the quark flavor is not identified, has been taking into account by the proper symmetrization of the matrix element squared to be evaluated for each event. The total measured cross-section is denoted by σ_{tot}. It will be parameterized according to Ref. [32] as:

$$\sigma_{\mathrm{tot}} \quad = \quad S_0 + S_1 \cdot \alpha + S_2 \cdot \alpha^2, \tag{2.3.4}$$

where α denotes generically any of the anomalous couplings under study.

The muon channel, with its selection cuts was used to evaluate the total cross section; one parameter fits were performed for different anomalous couplings. The

Model	Coupling	Value
$\hat{O}_{B_\phi}$	$x_\gamma \equiv \Delta\kappa_\gamma$	-0.0889 ± 0.0029
$\hat{O}_{W_\phi - B_\phi}$	$\delta_z \equiv \frac{\Delta g_Z^1}{\tan\theta_W}$	-0.1474 ± 0.0045
$\hat{O}_{W_\phi}$	$x_\gamma \equiv \Delta\kappa_\gamma$	-0.0420 ± 0.0017
$\hat{O}_W$	λ_γ	0.0654 ± 0.0017

Table 2.3.9: *Results on accuracy of TGB coupling estimation from ERATO for different models with just one free parameter.*

overall results are given in the Tab. 2.3.9 following the notation of [33] and [34]. The fact that the extracted couplings have a systematic bias is well understood and can be, in principle, corrected for by using the Monte Carlo predictions.

The proposed facility will cope with the demands W physics impose: limits on anomalous couplings of the order of 10^{-3} and W mass determination with accuracies better than 20 MeV are foreseen.

2.3.6 Study of $e^+e^- \rightarrow \chi_1^+ \chi_1^-$

Among the supersymmetric signal, chargino pair production $\chi_1^+ \chi_1^-$ at a linear collider operating at $\sqrt{s} = 500\,\text{GeV}$ is one of the most interesting. Discovery strategies at a linear collider have been discussed elsewhere [35, 36]. Here, the goal is to assess whether the anticipated detector performance poses any limitations to precisely determine the chargino mass $\chi_1^\pm$, and the mass of its supersymmetric decay product, the neutralino χ_1^0. Chargino production occurs via intermediate vector bosons γ, Z in the s channel and via electron-sneutrino exchange $\tilde{\nu}_e$ in the t channel. The reference reaction, the decay modes and the relevant SUSY mass parameters are

$$\begin{aligned}
e^+e^- &\rightarrow \chi_1^+ \chi_1^- \;, & & & (2.3.5)\\
\chi_1^\pm &\rightarrow \chi_1^0 \ell^\pm \nu & \text{BR} &= 34.5\,\% \quad \ell = e,\ \mu,\ \tau \;, & (2.3.6)\\
&\rightarrow \chi_1^0 q\bar{q}' & \text{BR} &= 65.5\,\% \;, & \\
m_{\chi_1^\pm} &= 168.2\,\text{GeV} \;, & & & (2.3.7)\\
m_{\chi_1^0} &= 88.1\,\text{GeV} \;, & & & (2.3.8)\\
m_{\tilde{\nu}_e} &= 304.0\,\text{GeV} \;. & & & (2.3.9)
\end{aligned}$$

The neutralino escapes detection, thus the experimental signature is a final state with an isolated lepton e or μ, two hadronic jets and missing energy. The cross section exhibits a typical threshold behavior proportional to β while the angular distribution is dominated by the very asymmetric t channel process: $d\sigma/d\cos\theta\chi_1^+$ is largest for $\cos\theta\chi_1^+ = -1$ and drops by a factor of ~ 5 at $\cos\theta\chi_1^+ = +1$. This behavior is quite different from Standard Model processes which may constitute a background to reaction (2.3.5). The shape of the angular distribution is essentially the same for the daughter-lepton and hadron-jets.

2.3.6.1 Simulation and Event Selection

Events are generated with the Monte Carlo program SPYTHIA [37], the supersymmetric extensions of PYTHIA with the JETSET fragmentation model. The center of mass energy is $\sqrt{s} = 500\,\mathrm{GeV}$ and the integrated luminosity is assumed to be $\mathcal{L} = 50\,\mathrm{fb}^{-1}$. Radiative corrections as well as beamstrahlung effects [30] are taken into account in the simulation. Charged particles are measured over the polar angle acceptance $|\cos\theta_{ch}| < 0.95$ with a momentum resolution of $\Delta p_\perp/p_\perp = 1.5\cdot 10^{-4}\,p_\perp\,[\mathrm{GeV}]$ and angular resolutions of $\Delta\theta = \Delta\phi = 0.001\,\mathrm{rad}$. The calorimetry extends over $|\cos\theta| < 0.99$ with an electro-magnetic energy resolution of $\Delta E_e/E_e = 0.10/\sqrt{E_e\,[\mathrm{GeV}]} \oplus 0.01$ and $\Delta E_h/E_h = 0.50/\sqrt{E_h\,[\mathrm{GeV}]} \oplus 0.04$ for hadrons. The event selection requires an isolated electron or muon, $\ell = \mathrm{e}$ or μ, and exactly two hadronic jets reconstructed with the JADE algorithm ($y_{\mathrm{cut}} = 0.01$). The event selection criteria for unpolarized $\mathrm{e}^\pm$ beams are listed in Tab. 2.3.10.

variable	accepted range
topology	one isolated lepton + two hadron jets
lepton $\ell = \mathrm{e}$ or μ	$5\,\mathrm{GeV} < E_\ell < 150\,\mathrm{GeV}$
	$-0.90 < Q_\ell \cos\theta_\ell < 0.50$
hadron jets	$5\,\mathrm{GeV} < E_j < 150\,\mathrm{GeV}$
	$\lvert\cos\theta_j\rvert < 0.90$
di-jet system	$10\,\mathrm{GeV} < E_{jj} < 175\,\mathrm{GeV}$
	$-0.90 < -Q_\ell \cos\theta_{jj} < 0.50$
	$m_{jj} < m_{\mathrm{W}} - 10\,\mathrm{GeV}$
recoil against di-jet system	$\lvert m_{\mathrm{recoil}-jj} - m_{\mathrm{W}}\rvert > 10\,\mathrm{GeV}$
missing momentum	$\lvert\cos\theta_{\vec{p}_{\mathrm{miss}}}\rvert < 0.90$

Table 2.3.10: *Event selection criteria for the reaction* $\mathrm{e}^+\mathrm{e}^- \to \chi_1^+\,\chi_1^-$, *leptons* $\ell = \mathrm{e}$ *or* μ.

The main background was found to come from

$$e^+e^- \rightarrow W\,W \rightarrow \ell\,\nu\;q\bar{q}' \qquad \ell = e,\ \mu,\ \tau\ . \tag{2.3.10}$$

Cascade decays $W \rightarrow \tau\,\nu$ with subsequent decays $\tau \rightarrow \mu\,\nu$ or $e\,\nu$ are included. The background from $e^+e^- \rightarrow W\,W$ production can be effectively suppressed by cuts on the signed lepton and quark polar angles (due to the V-A structure the $W^\pm$ and its decay fermions tend to be aligned along the $e^\pm$ direction, opposite to the preferred hemisphere of chargino production), on the di-jet mass and on the mass recoiling against the di-jet system around the W mass. The missing momentum vector $\vec{p}_{\rm miss}$ has to point into the detector acceptance in order to ensure good containment and to remove background from intermediate γ^*, Z decays produced by high energy radiated photons. The cross sections and efficiencies for the reference and background reactions are given in Tab. 2.3.11. The observable cross section for $e^+e^- \rightarrow \chi^+_1\,\chi^-_1$ leads to comfortable event rates. The acceptance of $\epsilon_{\ell jj} = 11.7\,\%$ is reasonably high, the biggest reduction factor originates from the decay branching fractions. The only relevant background from $e^+e^- \rightarrow W\,W$ amounts to $\sim 10\,\%$, other sources are negligible.

process	σ [fb]	BR($\ell\,\nu\;q\bar{q}'$)	$\epsilon_{\ell jj}$	$\sigma_{\rm acc}$ [fb]
$e^+e^- \rightarrow \chi^+_1\,\chi^-_1 \rightarrow \chi^0_1\,\ell\,\nu\;\chi^0_1\,q\bar{q}'$	245	0.293	0.117	28.7
$e^+e^- \rightarrow W\,W \rightarrow \ell\,\nu\;q\bar{q}'$	8000	0.292	$4{\cdot}10^{-4}$	3.2

Table 2.3.11: *Production cross sections, branching ratios, efficiencies and visible cross sections of the reference and background reactions, $\ell = $ e or μ.*

2.3.6.2 Mass Determination of $m_{\chi^\pm_1}$ and $m_{\chi^0_1}$

a) Di-jet Energy Spectrum

The masses of the chargino $m_{\chi^\pm_1}$ and the neutralino $m_{\chi^0_1}$ can be determined through the analysis of the di-jet system energy spectrum [36]. The SUSY parameters are chosen such that the chargino decays according to Eq. (2.3.6) via a virtual W into a three-body final state. The di-jet energy spectrum ranges between $25\,\mathrm{GeV} \leq E_{jj} \leq 156\,\mathrm{GeV}$. Here the situation is a bit more complicated with respect to the case of the scalar muon $e^+e^- \rightarrow \tilde{\mu}_R\,\tilde{\mu}_R$ discussed in the next section, where the two body decay implies that the endpoints from a flat energy distribution $\tilde{\mu}_R \rightarrow \chi^0_1\,\mu$ yield a better analyzing power toward the mass measurements. The observable di-jet energy spectrum, shown in Fig. 2.3.14, is distorted due to the event selection criteria, detector resolutions and initial state radiation, but still retains the characteristic features. The experimental energy resolution is expected to vary between $3\,\mathrm{GeV} \lesssim \Delta E_{jj} \lesssim 9\,\mathrm{GeV}$. Here again initial state radiation has practically no influence on the energy spectrum and mass determination; the photons carry away, on the average, very little energy with a rms spread of 3.4 GeV. Tails, however, are quite sizeable. Beamstrahlung effects are more important: they account for a sizeable c.m. energy reduction (CIRCE [30]) $\langle\sqrt{s}\rangle = 492.4\,\mathrm{GeV}$ with a rms width of 10.2 GeV at 500 GeV nominal value. The mass determination of $m_{\chi_1^\pm}$ and $m_{\chi_1^0}$ is obtained with a two parameter maximum likelihood fit to the di-jet energy spectra of Fig. 2.3.14; signal and background reactions (2.3.5) and (2.3.10) are included in the fitting procedure. The mass correlation with one and two standard deviation contours is displayed in Fig. 2.3.15. The result of the analysis is

$$\begin{aligned} m_{\chi_1^\pm}(\mathrm{obs},\ E_{jj}) &= 167.6 \pm 1.1\,\mathrm{GeV} \\ m_{\chi_1^0}(\mathrm{obs},\ E_{jj}) &= 88.2 \pm 0.6\,\mathrm{GeV}. \end{aligned}$$

The input values of Eqs. (2.3.7) and (2.3.8) are well reconstructed within the errors. With an integrated luminosity of $\mathcal{L} = 50\,\mathrm{fb}^{-1}$ the masses of the chargino $\chi_1^\pm$ and the neutralino χ_1^0 can both be measured with a statistical accuracy of $\Delta m/m \simeq 0.7\,\%$.

b) Threshold Energy Scan

Here, the chargino mass $m_{\chi_1^\pm}$ can be measured by determining the $\chi_1^+\chi_1^-$ production cross section close to the kinematic threshold. The cross section for $e^+e^- \to \chi_1^+\chi_1^-$ around the threshold including initial state radiation and beamstrahlung, but neglecting the finite chargino width, is shown in Fig. 2.3.16. The excitation curve rises steeply $\propto \beta$. It is assumed to collect $\mathcal{L} = 10\,\mathrm{fb}^{-1}$ at five different c.m. energies to cover the range from $\sqrt{s} = 336\,\mathrm{GeV}$ to $\sqrt{s} = 341\,\mathrm{GeV}$. A χ^2 analysis of the threshold scan yields a statistical sensitivity to the chargino mass of

$$m_{\chi_1^\pm}(\mathrm{obs}, \mathrm{scan}) = 168.2 \pm 0.100\,\mathrm{GeV}\ .$$

The scanning strategy has not been optimized concerning the luminosity weighting. A cross section measurement at the kinematic threshold offers the possibility to improve the precision attainable on the chargino mass $m_{\chi_1^\pm}$ by an order of magnitude already with a moderate integrated luminosity.

c) Polarized Beams

Longitudinally polarized beams offer great advantages for the study of SUSY phenomenology. The linear collider might provide polarizations up to $P_L(e^-) = \pm 0.90$ and

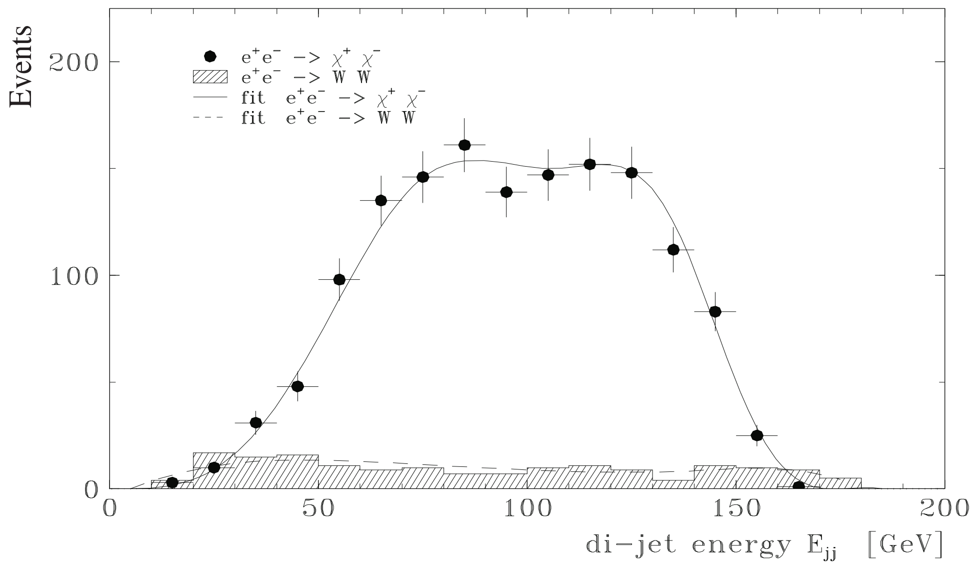

Figure 2.3.14: *Di-jet energy spectra E_{jj} of the reaction* $e^+e^- \to \chi_1^+\chi_1^-$ *(• and —) and the background reaction* $e^+e^- \to W\,W$ *(histogram and −−), assuming* $\mathcal{L} = 50\,\mathrm{fb}^{-1}$.

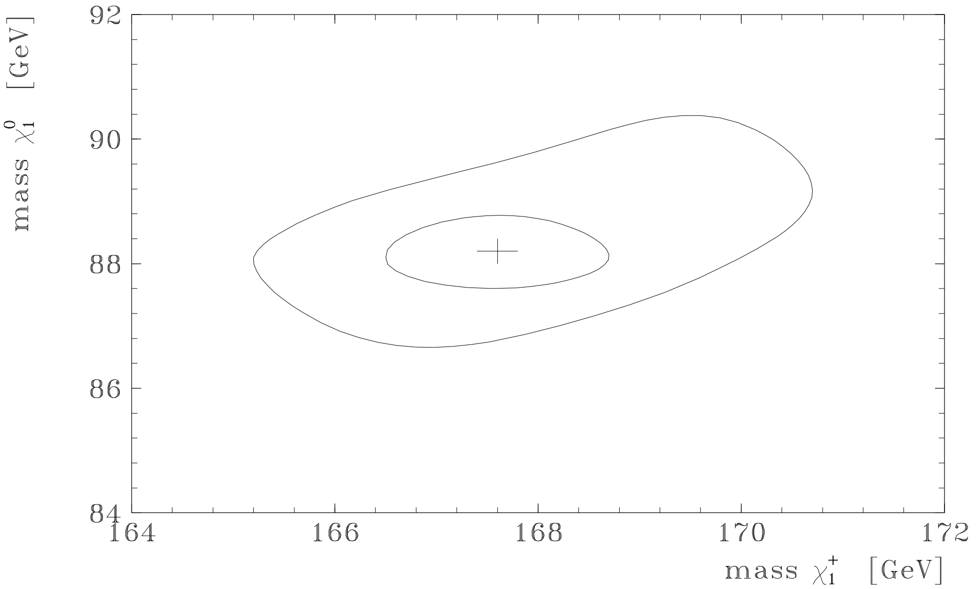

Figure 2.3.15: *Correlation of* $m_{\chi_1^0}$ *versus* $m_{\chi_1^\pm}$ *from a two parameter mass fit. The reconstructed masses are indicated by the cross, the contours show the one standard deviation and two standard deviations measurements.*

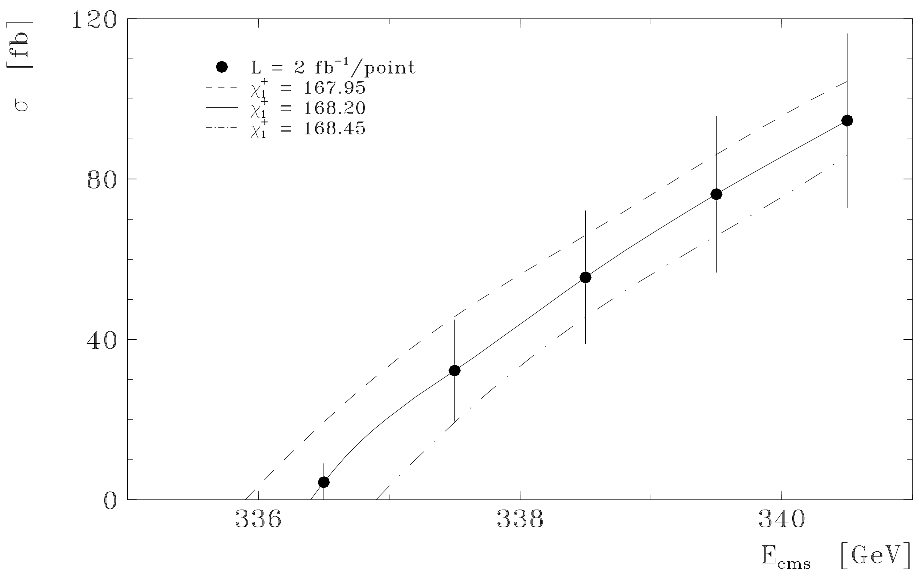

Figure 2.3.16: *Cross section for* $e^+e^- \to \chi_1^+\chi_1^-$ *around the kinematic threshold with initial state radiation and beamstrahlung, assuming* $\mathcal{L} = 2\,\mathrm{fb}^{-1}$ *per measurement* (•). *The curves indicate chargino masses of* $m_{\chi_1^\pm} = 168.2 \pm 0.25\,\mathrm{GeV}$.

$P_L(e^+) = \pm 0.60$. In terms of background rejection chargino production does not benefit from polarization as the scalar lepton production does. For left-handed electrons the cross section σ_L increases by a factor of ~ 1.7, while for right-handed electrons the cross section σ_R decreases by almost an order of magnitude. This is due to the fact that, for the chosen set of SUSY parameters, $\chi_1^+\chi_1^-$ production is dominated by $\tilde{\nu}_e$ t channel exchange, which couples only to left-handed electrons. The W W cross section scales by approximately the same amount. Polarization, however, is indeed useful because it offers the possibility of disentangling the s and t channel diagrams and to determine the gaugino and higgsino components of the chargino: $\chi_1^\pm = \alpha\,\tilde{\mathrm{W}}^\pm + \beta\,\tilde{\mathrm{H}}^\pm$, where the higgsino couples only to right-handed electrons. With a luminosity of $\mathcal{L} = 10\,\mathrm{fb}^{-1}$ the cross section σ_L can be measured with a statistical accuracy of $\Delta\sigma_L \sim 4.5\,\%$ and σ_R with a statistical error of $\Delta\sigma_R \sim 15\,\%$. Thus, precise measurements of σ_L and σ_R will allow the chargino mixing parameters to be determined. Doing this at the same time as measuring the sparticle masses will give important tests of the predictions of SUSY-GUT theories.

The masses of the chargino and neutralino can be determined by a study of the reaction $e^+e^- \to \chi_1^+\chi_1^-$. The event signature is an isolated lepton $\ell = e$ or μ and two hadron jets. The detection efficiency is reasonably high and clean event samples can be obtained. The main background from $e^+e^- \to W\,W$ is small. The energy spectrum of the di-jet system provides a powerful tool to measure the chargino and neutralino masses. With an integrated luminosity of $\mathcal{L} = 50\,\mathrm{fb}^{-1}$ at a center of mass energy $\sqrt{s} = 500\,\mathrm{GeV}$ the expected accuracy is

$$\begin{aligned} \Delta m_{\chi_1^\pm} &\simeq 1.1\,\mathrm{GeV}\ , \\ \Delta m_{\chi_1^0} &\simeq 0.6\,\mathrm{GeV}\ . \end{aligned}$$

A more accurate chargino mass $m_{\chi_1^\pm}$ may be obtained by a $\chi_1^+\chi_1^-$ production cross section measurement around the kinematic threshold. The expected sensitivity is $\Delta m_{\chi_1^\pm} \sim \mathcal{O}(100\,\mathrm{MeV})$, depending on the collected statistics. No experimental limitation is expected with the experimental apparatus described in this report.

2.3.7 Study of $e^+e^- \to \tilde{\mu}_R\,\tilde{\mu}_R$

The last reaction to be discussed in this section is the production of scalar muons $\tilde{\mu}_R$. Previous studies concentrated on the discovery potential of lepton colliders at $\sqrt{s} = 500\,\mathrm{GeV}$ [35]. Here, the main thrust is in trying to devise methods to precisely determine the mass of the scalar muon $\tilde{\mu}_R$ and of its (supersymmetric) decay product, the neutralino χ_1^0. The reference reaction and the relevant SUSY mass parameters are

$$e^+e^- \to \tilde{\mu}_R^+\tilde{\mu}_R^-\ , \tag{2.3.11}$$

$$\tilde{\mu}_R \to \mu\,\chi_1^0 \qquad \mathrm{BR} = 99.5\,\%\ , \tag{2.3.12}$$

$$m_{\tilde{\mu}_R} = 275.1\,\mathrm{GeV}\ , \tag{2.3.13}$$

$$m_{\chi_1^0} = 88.1\,\mathrm{GeV}\ . \tag{2.3.14}$$

The neutralino escapes detection, thus the experimental signature is an acoplanar $\mu^+\,\mu^-$ pair and missing energy. The cross section exhibits a typical threshold behavior $\propto \beta^3$ and has a characteristic polar angle distribution $\propto \sin^2\theta$, quite different from Standard Model processes which may constitute a background to reaction (2.3.11).

2.3.7.1 Simulation and Event Selection

Events are generated with the Monte Carlo code SPYTHIA [37], which includes supersymmetric extensions of PYTHIA; the JETSET fragmentation model is included. The center of mass energy is $\sqrt{s} = 800\,\mathrm{GeV}$; the assumed integrated luminosity is $\mathcal{L} = 125\,\mathrm{fb}^{-1}$. QED radiative corrections as well as beamstrahlung effects [30] are taken into account. The detector simulation follows the proposed design and assumes μ detection over 95 % of the total solid angle ($|\cos\theta_\mu| < 0.95$) with a momentum resolution of $\Delta p_\perp/p_\perp = 1.5\cdot 10^{-4}\,p_\perp$ [GeV] and an angular resolution of $\Delta\theta_\mu = \Delta\phi_\mu = 0.001$ rad. The event selection requires an acoplanar $\mu^+\,\mu^-$ pair (the acoplanarity is defined as the difference between the lepton azimuthal angles ϕ_μ measured in the plane perpendicular to the $e^\pm$ beams) and nothing else in the detector. The event selection criteria for unpolarized $e^\pm$ beams are listed in Tab. 2.3.12. The following background sources

variable	accepted range
topology	$\mu^+ \mu^-$ pair + nothing else in detector
radiative γ veto	$E_\gamma > 1\,\mathrm{GeV}$ $\quad \lvert \cos\theta_\gamma \rvert < 0.985$
lepton polar angle	$\lvert \cos\theta_\mu \rvert < 0.95$
at least one lepton	$Q_\mu \cos\theta_\mu < 0.75$
acoplanarity	$\lvert \phi_{\mu^+} - \phi_{\mu^-} \rvert < 145°$
missing momentum	$\lvert \cos\theta_{\vec{p}_{\mathrm{miss}}} \rvert < 0.90$
lepton energy	$45\,\mathrm{GeV} < E_\mu < 375\,\mathrm{GeV}$
di-lepton mass	$\lvert m_{\mu^+\mu^-} - m_{\mathrm{Z}} \rvert > 10\,\mathrm{GeV}$
recoil mass	$\lvert m_{\mathrm{recoil}} - m_{\mathrm{Z}} \rvert > 15\,\mathrm{GeV}$

Table 2.3.12: *Event selection criteria for the reaction* $e^+e^- \to \tilde{\mu}_R \tilde{\mu}_R$.

are considered in the analysis

$$e^+e^- \to \gamma/Z \to \mu^+ \mu^- (\gamma)\,, \tag{2.3.15}$$

$$e^+e^- \to Z\,Z \to \mu^+ \mu^- \nu\,\nu\,, \tag{2.3.16}$$

$$e^+e^- \to W\,W \to \mu^+ \nu\, \mu^- \nu\,. \tag{2.3.17}$$

Cascade decays γ, $Z \to \tau\,\tau$ and $W \to \tau\,\nu$ with subsequent decays $\tau \to \mu\,\nu$ are included. The missing momentum vector $\vec{p}_{\mathrm{miss}}$ has to point to the sensitive area of the detector in order to ensure good containment and to suppress background from intermediate Z decays produced by high energy radiated photons. Further reduction of Z background is obtained with cuts on the di-lepton invariant mass and on the recoil mass close to the Z pole. Background from $e^+e^- \to W\,W$ production can be effectively suppressed by cuts on the signed lepton polar angle (due to the V-A structure the $W^\pm$ and its decay $\mu^\pm$ tend to be aligned along the $e^\pm$ direction) and on the acoplanarity. The cross sections and efficiencies for the reference and background reactions are given in Tab. 2.3.13. The observable cross section for $e^+e^- \to \tilde{\mu}_R \tilde{\mu}_R$ leads to comfortably large and clean event rates, the acceptance, $\epsilon_{\mu^+\mu^-} = 50\,\%$, being reasonably high. The most prominent background contamination comes from $e^+e^- \to W\,W$ and amounts to $\sim 10\,\%$, the other backgrounds are negligible.

process	σ [fb]	$\epsilon_{\mu^+\mu^-}$	σ_{acc} [fb]
$e^+e^- \to \tilde{\mu}_R^+\tilde{\mu}_R^- \to \mu^+\chi_1^0\,\mu^-\chi_1^0$	15.2	0.50	7.6
background			
$e^+e^- \to \gamma/Z \to \mu^+\mu^-(\gamma)$	850	$< 3\cdot 10^{-5}$	< 0.03
$e^+e^- \to Z\,Z \to \mu^+\mu^-\,\nu\,\nu$	5.9	$1.3\cdot 10^{-2}$	0.08
$e^+e^- \to W\,W \to \mu^+\nu\,\mu^-\nu$	210	$3.8\cdot 10^{-3}$	0.8
total			~ 0.9

Table 2.3.13: *Production cross sections, efficiencies and visible cross sections of the reference and background reactions. Cascade decays* γ, $Z \to \tau\,\tau$, $W \to \tau\,\nu$ *and* $\tau \to \mu\,\nu$ *are included.*

2.3.7.2 Mass Determination of $m_{\tilde{\mu}_R}$ and $m_{\chi_1^0}$

The masses of the scalar muon $\tilde{\mu}_R$ and the neutralino χ_1^0 can be evaluated by analyzing the energy spectrum of the final state leptons $\mu^\pm$. The scalar muon decays isotropically according to the decay mode (2.3.12) and the simple two-body kinematics results in a flat energy distribution of the observable muon. The endpoint energies E_μ^{min} and E_μ^{max} can be related to the masses of the scalar muon and the neutralino via

$$\frac{m_{\tilde{\mu}_R}}{2}\left(1-\frac{m_{\chi_1^0}^2}{m_{\tilde{\mu}_R}^2}\right)\gamma\,(1-\beta) \;\le\; E_\mu \;\le\; \frac{m_{\tilde{\mu}_R}}{2}\left(1-\frac{m_{\chi_1^0}^2}{m_{\tilde{\mu}_R}^2}\right)\gamma\,(1+\beta)\;, \quad (2.3.18)$$

$$49.1\,\mathrm{GeV} \;\le\; E_\mu \;\le\; 309.8\,\mathrm{GeV}\;,$$

where $\gamma = \sqrt{s}\,/\,(2\,m_{\tilde{\mu}_R})$ and $\beta = \sqrt{1-\gamma^{-2}}$. The observable lepton energy spectrum, shown in Fig. 2.3.17, is distorted due to the event selection criteria, detector resolution and initial state radiation, but still maintains the characteristic features. The experimental energy resolution is expected to vary between $0.5\,\mathrm{GeV} \lesssim \Delta E_\mu \lesssim 15\,\mathrm{GeV}$. Initial state radiation has very little influence on the shape of the energy spectrum and the mass determination ($\langle\sqrt{s}\rangle = 799.8\,\mathrm{GeV}$, rms spread 3.6 GeV with a very long tail). However, the beamstrahlung effects are more important and must be kept under control. In the present version of CIRCE [30] the mean center of mass energy is reduced to $\langle\sqrt{s}\rangle = 788.9\,\mathrm{GeV}$ with a rms of 17.4 GeV. The mass determination of $m_{\tilde{\mu}_R}$ and $m_{\chi_1^0}$ has been obtained by performing a two parameter maximum likelihood fit to

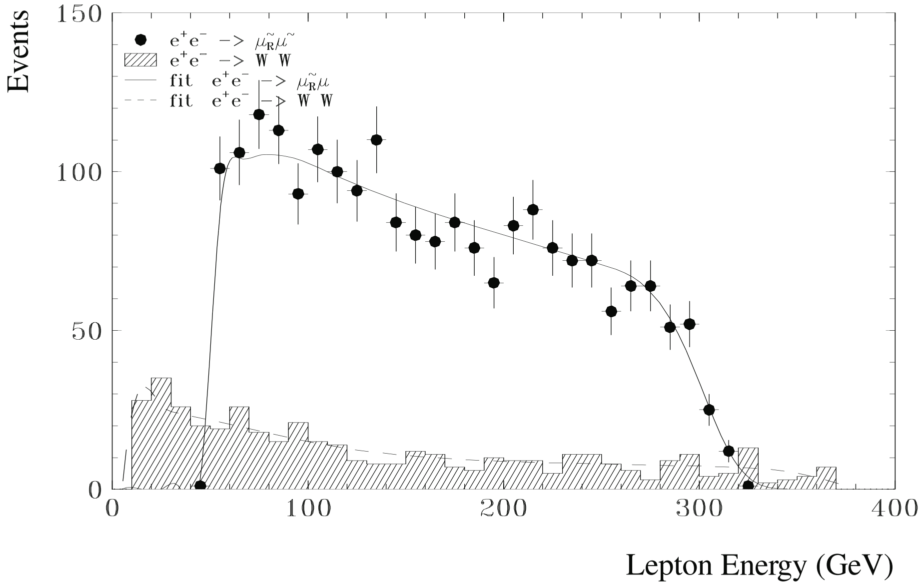

Figure 2.3.17: *Energy spectra of the final state* $\mu^{\pm}$ *for the reaction* $\mathrm{e^+e^-} \to \tilde{\mu}_R\,\tilde{\mu}_R$ *(●) and the background* $\mathrm{e^+e^-} \to \mathrm{W\,W}$ *(histogram), assuming* $\mathcal{L} = 125\,\mathrm{fb}^{-1}$*.*

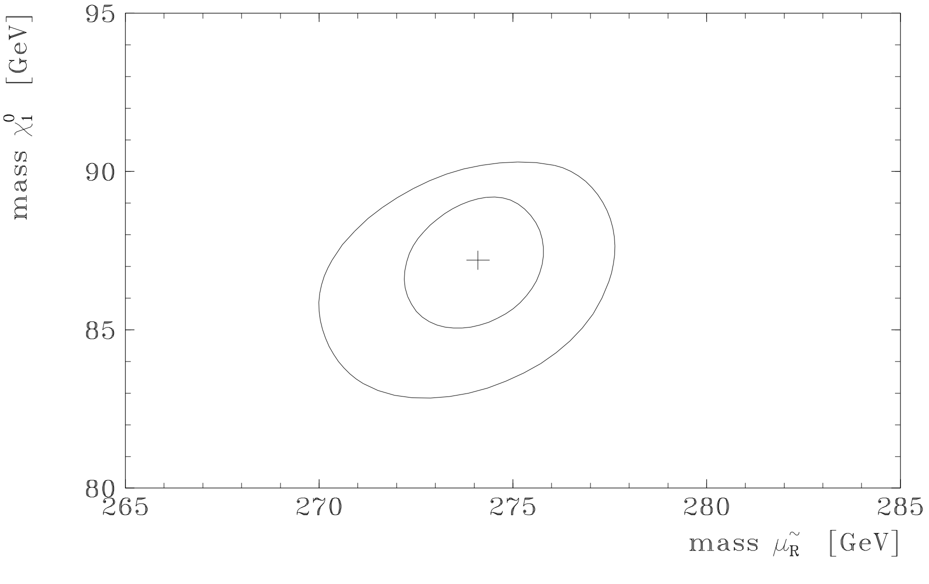

Figure 2.3.18: *Correlation of* $m_{\chi_1^0}$ *versus* $m_{\tilde{\mu}_R}$ *from a two parameter mass fit using unpolarized beams. The reconstructed masses are indicated by the cross, the contours show the one standard deviation and two standard deviation measurements.*

the lepton spectra of Fig. 2.3.17 including the signal and background reactions (2.3.11) and (2.3.17). The mass correlation with one and two standard deviation contours is shown in Fig. 2.3.18. The final result is

$$\begin{aligned} m_{\tilde{\mu}_R}\,(\mathrm{obs}) &= 274.1\ ^{+1.7}_{-1.9}\,\mathrm{GeV}\ , \\ m_{\chi^0_1}\,(\mathrm{obs}) &= 87.2\ ^{+2.1}_{-2.4}\,\mathrm{GeV}\ . \end{aligned} \tag{2.3.19}$$

Comparing this mass determination with the input values of Eqs. (2.3.13) and (2.3.14) one observes a small shift towards lower masses, but well within the errors. With a luminosity of $\mathcal{L} = 125\,\mathrm{fb}^{-1}$ the masses of the scalar muon $\tilde{\mu}_R$ and the lightest neutralino χ^0_1 can be measured with a statistical accuracy of $\Delta m_{\tilde{\mu}_R}/m_{\tilde{\mu}_R} \simeq 0.7\,\%$ and $\Delta m_{\chi^0_1}/m_{\chi^0_1} \simeq 2.5\,\%$.

a) Use of Polarized Electrons

The linear collider offers the possibility of accelerating longitudinally polarized electrons: this technique carries enormous advantages for the study of SUSY phenomenology. A right-handed electron with a degree of polarization $P_L(\mathrm{e}^-) = +0.90$ (such a large polarization might be attainable by the time the linear collider is completed) enhances the cross section $\sigma(\mathrm{e}^+\mathrm{e}^-_\mathrm{R} \to \tilde{\mu}_R\,\tilde{\mu}_R)$ by a factor of ~ 1.6. At the same time the most severe background, W pair production, is suppressed by an order of magnitude. The background suppression allows, in turn, the cuts to be relaxed on the polar angle of the signed lepton and on the acoplanarity, increasing the acceptance to $\epsilon_{\mu^+\,\mu^-} \simeq 0.60$. Overall, the gain is equivalent to almost doubling the integrated luminosity. The muon energy spectrum, displayed in Fig. 2.3.19, is more uniform than in the unpolarized case. Such an event sample, essentially background free, would allow the mass errors to be reduced, in particular for the scalar muon. The expected precision is

$$\begin{aligned} m_{\tilde{\mu}_R}\,(\mathrm{obs},\,\mathrm{e}^-_R) &= 275.3\ ^{+0.9}_{-0.7}\,\mathrm{GeV}\ , \\ m_{\chi^0_1}\,(\mathrm{obs},\,\mathrm{e}^-_R) &= 88.2\ ^{+1.8}_{-1.6}\,\mathrm{GeV}\ . \end{aligned}$$

The masses correlation with one and two standard deviation contours is shown in Fig. 2.3.20.

b) Alternative Determination of $m_{\tilde{\mu}_R}$

An alternative to determine the scalar muon mass $m_{\tilde{\mu}_R}$ is to measure the $\tilde{\mu}_R\,\tilde{\mu}_R$ production cross section close to the kinematic threshold with a similar technique as proposed for the W W and $\mathrm{t}\bar{\mathrm{t}}$ pair production. The lepton energy spectrum becomes almost monochromatic, a spectacular signature. A threshold scan has the additional advantage that the signal reaction is not spoiled by complicated cascade decays, which otherwise may be kinematically allowed. The cross section for $\mathrm{e}^+\mathrm{e}^-_\mathrm{R} \to \tilde{\mu}_R\,\tilde{\mu}_R$ around the

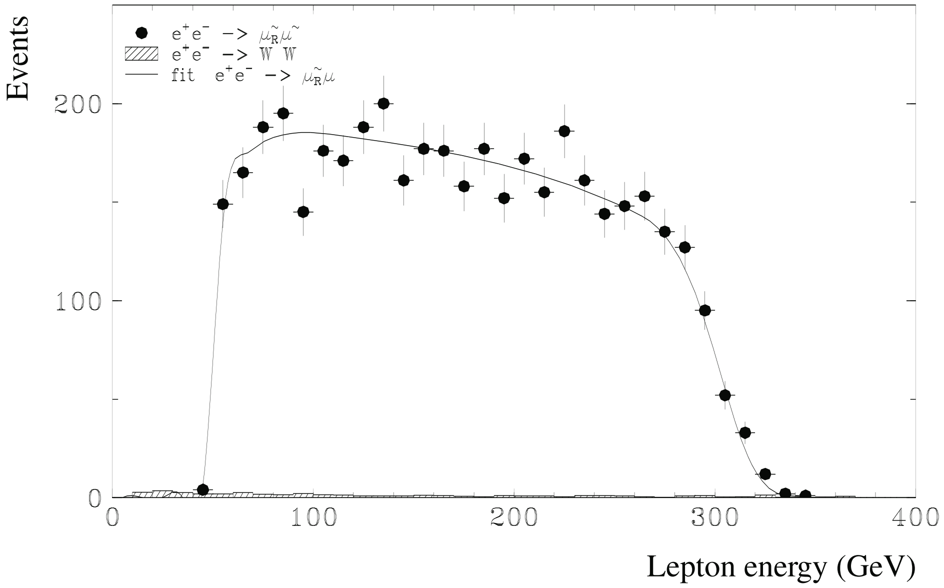

Figure 2.3.19: *Energy spectra of the final state* $\mu^\pm$ *for the reaction* $\mathrm{e}^+\mathrm{e}^-_\mathrm{R} \to \tilde{\mu}_R\,\tilde{\mu}_R$ *(•) and the background* $\mathrm{e}^+\mathrm{e}^-_\mathrm{R} \to \mathrm{W\,W}$ *(histogram), assuming* $\mathcal{L} = 125\,\mathrm{fb}^{-1}$.

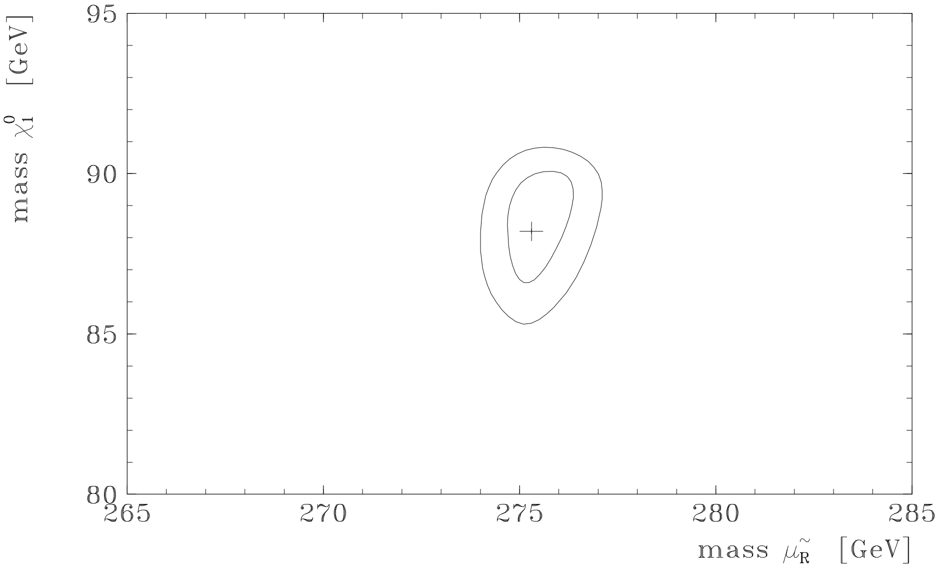

Figure 2.3.20: *Correlation of* $m_{\chi^0_1}$ *versus* $m_{\tilde{\mu}_R}$ *from a two parameter mass fit using a polarized* e^-_R *beam. The reconstructed masses are indicated by the cross, the contours show the one standard deviation and two standard deviation measurements.*

threshold using right-handed electrons ($P_L = +0.90$) and ignoring beamstrahlung is shown in Fig. 2.3.21 a). The excitation curve rises as β^3, slower than for spin 1/2 particles. An event sample of $\mathcal{L} = 100\,\mathrm{fb}^{-1}$ integrated luminosity equally shared between 10 measurements in the center of mass energy range $\sqrt{s} = 550\,\mathrm{GeV}$ to $\sqrt{s} = 560\,\mathrm{GeV}$ is assumed. A χ^2 analysis of the threshold scan, results shown in Fig. 2.3.21 b), yields a statistical sensitivity to the scalar muon mass of

$$m_{\tilde{\mu}_R}(\mathrm{obs},\, \mathrm{e}_R^-) \quad = \quad 275.1\,^{+0.35}_{-0.30}\,\mathrm{GeV} \ .$$

No attempt has been yet done to optimize the choice of beam energy settings and integrated luminosities; also, beamstrahlung effects have not be taken into account. Nevertheless, a cross section measurement at the kinematic threshold without significant background allows an improvement on the the scalar muon mass measurement $m_{\tilde{\mu}_R}$ of a factor between two and three with respect to the other technique discussed.

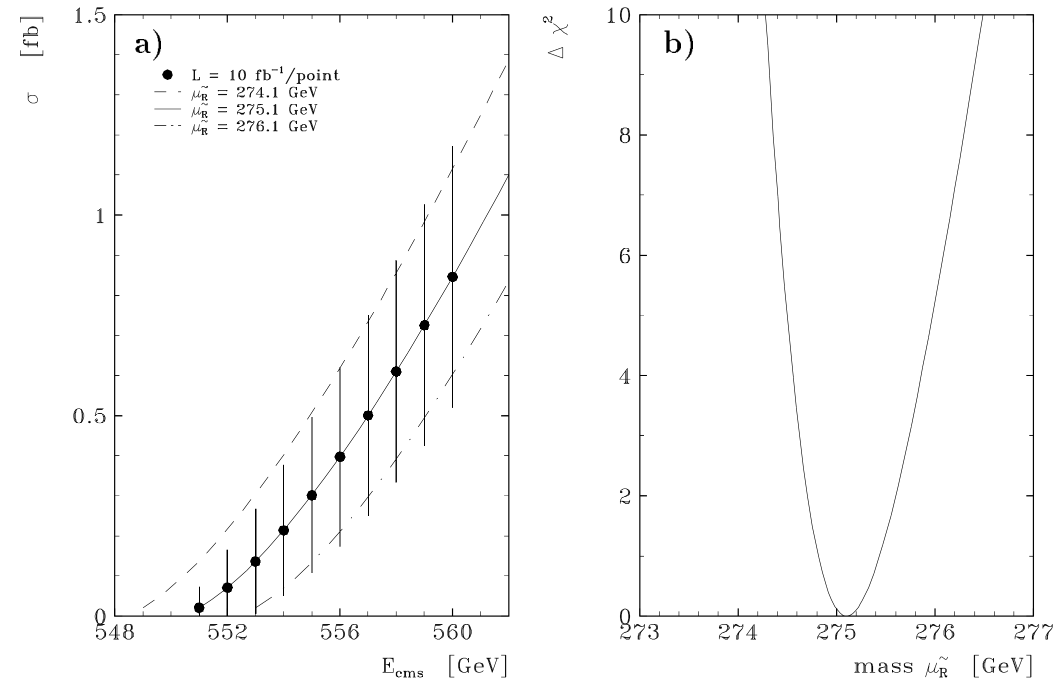

Figure 2.3.21: *a) Cross section for* $\mathrm{e}^+\mathrm{e}^-_\mathrm{R} \to \tilde{\mu}_R\,\tilde{\mu}_R$ *around the kinematic threshold without beamstrahlung effects, assuming* $\mathcal{L} = 10\,\mathrm{fb}^{-1}$ *per measurement (•). The curves indicate scalar muon masses of* $m_{\tilde{\mu}_R} = 275.1 \pm 1.0\,\mathrm{GeV}$. *b) Result of a* χ^2 *analysis versus* $m_{\tilde{\mu}_R}$.

To summarize, the study of the reaction $\mathrm{e}^+\mathrm{e}^- \to \tilde{\mu}_R^+\,\tilde{\mu}_R^- \to \mu^+\,\chi_1^0\,\mu^-\,\chi_1^0$ carried out with the proposed detector will lead to the precise determination of the scalar muon $\tilde{\mu}_R$ and neutralino χ_1^0 masses. With simple selection criteria a reasonably high detection efficiency and clean event samples can be obtained; the background is expected to be small and manageable. The energy spectrum of the decay lepton provides a very powerful tool to measure masses. Collecting a luminosity of $\mathcal{L} = 125\,\mathrm{fb}^{-1}$ and using unpolarized beams at a center of mass energy of $\sqrt{s} = 800\,\mathrm{GeV}$ the expected mass accuracy is $\Delta m_{\tilde{\mu}_R} \simeq 1.8\,\mathrm{GeV}$ and $\Delta m_{\chi_1^0} \simeq 2.3\,\mathrm{GeV}$. The use of right-handed polarized electrons turns out to be extremely valuable. The signal can be enhanced by almost a factor of two and the main background (W pair production) can be suppressed by an order of magnitude. The same integrated luminosity, with e_R^- beam 90 % right-handed polarized, would allow mass determinations with a precision of

$$
\begin{aligned}
\Delta m_{\tilde{\mu}_R} &\simeq 0.8\,\mathrm{GeV}\ , \\
\Delta m_{\chi_1^0} &\simeq 1.7\,\mathrm{GeV}\ .
\end{aligned}
$$

An even more accurate mass measurement of the scalar muon $\tilde{\mu}_R$ may be obtained by a $\tilde{\mu}_R\,\tilde{\mu}_R$ production cross section scan around the kinematic threshold. Again polarized electrons are very important. The expected sensitivity is $\Delta m_{\tilde{\mu}_R} \sim \mathcal{O}\,(350\,\mathrm{MeV})$. More sophisticated simulations, including beamstrahlung, for the threshold scan are in progress. The physics reach for this measurement is not limited by detector performances. Beamstrahlung effects, however, might be more dangerous in impairing the physics reach of this measurement and other relying on reconstructing threshold behavior of the cross section.

2.3.8 Conclusions

The design of the detector for the next generation of electron colliders, as described in this chapter was tested evaluating its performances through detailed Monte Carlo simulations. Five different reactions were selected on the basis of both physics relevance and experimental peculiarities:

- The study of top production and decay at threshold, a topic of great physics relevance: the expected experimental reach of the linear collider will give a $\approx$ 0.1 % precision in the mass measurement. From the experimental point of view this process depends upon the ability of the apparatus to reconstruct multijet events and extract invariant masses of combinations of jets. A reasonable capability for tagging detached vertices is needed. Beamstrahlung phenomena have to be kept under control and measured during data taking. The proposed set-up should be able to measure the top mass to better than 110 MeV; the total top width is expected to be measured with a relative precision smaller that 20 %. As a by-product of this measurement, α_s would be measured to a relative precision better than 3 %. The luminosity required is of the order of $50\,\mathrm{fb}^{-1}$.

- If the Higgs boson mass is in the region below the WW threshold the linear collider will have important contributions to make. This study has shown that our chosen detector can measure the total cross section for production of the standard model Higgs boson in this region with good precision, and recognize its decay products. The quality of the vertex detector and the tracking system are particularly important for measuring branching ratios to discriminate between the Higgs bosons predicted by different models.

- The associate production of H and A bosons was chosen also to check the capabilities of the detector both on detached vertices identification and on jet detection and reconstruction. The proposed apparatus will detect and identify the H A production in the mass range up to 340 GeV if the collider will deliver $\approx 200\,\mathrm{fb}^{-1}$ at 800 GeV total energy; the H A signal can, however, be identified also at reduced luminosity ($50\,\mathrm{fb}^{-1}$) with a less precise measurement of the production cross section.

- W pair production, with its very forward peaked angular distribution, requires good angular coverage and good resolution on the momentum (and charge where possible) of tracks going into the forward regions, especially leptons. With the proposed detector and integrated luminosity of $50\,\mathrm{fb}^{-1}$ at 500 GeV E_{cm} limits on the anomalous couplings of the order of 10^{-3} will be reached.

- The linear collider will be particularly suited to the study of lepton and gauge boson superpartners, at whatever mass they are to be found. These studies have shown that if smuons and/or charginos are kinematically accessible at any part of the energy range of the machine then they can be identified and their masses can be measured to better than 1 %.

The overall performance of the detector described in section 2.2 is, on the basis of this selected set of reference reactions, more than adequate to give a uniquely important programme of measurements. Most of the studies have shown that the sensitivity will be limited either by statistics or by such unavoidable features of the detector as the loss of particles close to the forward direction. There is still scope for more detailed studies, including other physics processes and using full GEANT simulation in places, to refine the design and point to regions where further detector R & D will be needed.

Bibliography

[1] H.J. Schreiber, code SIMDET, available upon request from "schreibe@ifh.de"

[2] G.W. Wilson, talk to the ECFA/DESY workshop at MPI-Munich, 16-17 September 1996.

[3] G. Crawford et al. (the CLEO II collaboration), "Luminosity measurement with the CLEO II detector", Nucl. Instrum. and Meth. A345 (1994) 429-439.

[4] S. Jadach and B. Ward, private communication.

[5] M.N. Frary, D.J. Miller, "Monitoring the Luminosity Spectrum", DESY 92-123A, p. 379.

[6] N. Toomi, J. Fujimoto, S. Kawabata, Y. Kurihara, "Luminosity measurement in future e^+e^- linear colliders using large angle Bhabha events", KEK-CP-051, November 1996.

[7] T. Sjöstrand, Comp. Phys. Comm. 84 (1994) 74.

[8] S. Bethke, Z. Kunszt, D.E. Soper, W.J. Stirling, "New Jet Algorithms: Next-to-leading Order QCD and Hadronization Corrections", CERN-TH 6222/91.

[9] P. Comas et al., "The physics of the e^+e^- threshold scan" in: Proceedings of the Workshop on e^+e^- collisions at TeV energies: the Physics Potential, Annecy, Gran Sasso, Hamburg, February to September 1995, ed. P.M. Zerwas, DESY Report 96-123d, pp. 57–66.

[10] A. Venturi, in: Proceedings of the Workshop on e^+e^- Collisions at 500 GeV: The Physics Potential Munich, Annecy, Hamburg, November 1992 to April1993, ed. P.M. Zerwas, DESY Report 93-123c, pp. 269–281.

[11] M. Schmitt, "Top Production and Decay Form Factors" in: Proceedings of the Workshop on e^+e^- collisions at TeV energies: the Physics Potential, Annecy, Gran Sasso, Hamburg, February to September 1995, ed. P.M. Zerwas, DESY Report 96-123d, pp. 67–74.

[12] M. Martinez and S. Orteu, "Direct measurement of the top quark Yukawa coupling", in: Proceedings of the Workshop on e^+e^- collisions at TeV energies: the Physics Potential, Annecy, Gran Sasso, Hamburg, February to September 1995, ed. P.M. Zerwas, DESY Report 96-123d, pp. 75–82.

[13] G. Blair, to appear in DESY 97-123E.

[14] P.M. Zerwas, in: Proc. of the International Conference on High Energy Physics, Marseille, 1993;
A. Djouadi, Int. Mod. Phys. A10 (1995) 1.

[15] J. Kamoshita et al., in: Proc. of the Workshop on Physics and Experiments with Linear Colliders, Vol. II, World Scientific, Singapore 1996.

[16] A. Djouadi, M. Spira and P.M. Zerwas, DESY 95-210.

[17] P. Grosse-Wiesmann, D. Haidt and H.J. Schreiber, DESY 92-123A;
P. Janot, LAL 93-38;
H.D. Hildreth, T.L. Barklow and D.L. Burke, Phys. Rev. D49 (1994), 3441.

[18] M. Sachwitz, H.J. Schreiber and S. Shichanin, to appear in DESY 95-123E.

[19] M. Battaglia and R. Vuopionperä, to appear in DESY 97-123E.

[20] P. Janot, "The HZHA generator", in Physics at LEP2, Eds. G.Altarelli, T. Sjostrand and F. Zwirner, CERN 96-01, Vol.2, p. 309.

[21] F.A. Berends, R.Kleiss and R. Pittau, Nucl. Phys. B424 (1994) 308; Nucl. Phys. B426 (1994) 344.

[22] C.Troncon, "Tagging Heavy Flavours with Vertex Detectors at e^+e^- Colliders", Proceedings of 5th International Workshop on Vertex Detectors, VERTEX 96, Chia, Cagliari, Italy, 16/21 June 1996, to be published on Nucl. Instrum. and Meth.

[23] D. Brown, M. Frank, "Tagging b hadrons using track impact parameters", ALEPH 92-135, PHYSIC 92-124;
ALEPH Collab., D. Buskulic et al., Phys. Lett. B313 (1993), 535.

[24] DELPHI Collab., P. Abreu et al., Zeitschr. f. Phys. C65 (1995), 555;
DELPHI Collab., P. Abreu et al., Nucl. Instrum. and Meth. A378 (1996) 57;
G.V.Borisov, "Lifetime Tag of events $Z \to b\bar{b}$ with the DELPHI Detector", DELPHI 94-125/PROG 208, 1994.

[25] A. Andreazza and C. Troncon, to appear in DESY 97-123E.

[26] E. Boos et al., Moscow State University preprint SNUTP-94-116, Oct. 1994 and Korean Physical Society meeting, Oct. 21 1994, hep-ph/9503280.

[27] C. Papadopoulos, DEMO-HEP-96/02 and hep-ph/96099320, September 1996.

[28] H. Anlauf et al., Manual of WOPPER version 1.5.

[29] M.S. Skrypzek et al., Comp. Phys. Comm. 94 (1996) 216.

[30] T. Ohl, IKDA 96/13, hep-ph/9607454, July 1996.

[31] Z. Kunszt, Phys. Lett. 99B (1981) 429.

[32] C. Papadopoulos, Phys. Lett. B352 (1995) 144.

[33] M. Bilenky et al., Nucl. Phys. B409 (1993) 22.

[34] "Physics at LEP2", Vol.1, CERN 96-01 Yellow Report, edited by G. Altarelli, T. Sjöstrand and F. Zwirner, Geneva, February 1996.

[35] Proceedings of the Workshop on e^+e^- Collisions at 500 GeV: The Physics Potential, Munich, Annecy, Hamburg, November 1992 to April 1993, ed. P.M. Zerwas, DESY Report 93-123 A+B and DESY 93-123 C.

[36] T. Tsukamoto et al., Phys. Rev. D 51 (1995) 3153.

[37] S. Mrenna, "SPYTHIA, A Supersymmetric Extension of PYTHIA 5.7", ANL-HEP-PR-96-63 and hep-ph/9609360;
T. Sjöstrand, "PYTHIA 5.7 and JETSET 7.4, Physics and Manual", CERN-TH 7712/93.